

Neutron-Deuteron Breakup and Quasielastic Scattering

by

Alice Elisabeth Ohlson

Submitted to the Department of Physics
in partial fulfillment of the requirements for the degree of

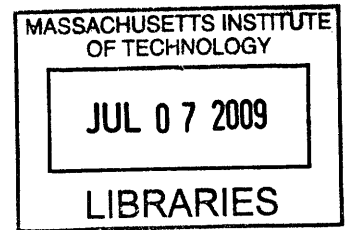
Bachelor of Science in Physics

at the

MASSACHUSETTS INSTITUTE OF TECHNOLOGY

June 2009


© Massachusetts Institute of Technology 2009. All rights reserved.



Author

Department of Physics
May 8, 2009

Certified by

 June Matthews
Professor of Physics
Thesis Supervisor

Accepted by

Professor David E. Pritchard
Senior Thesis Coordinator, Department of Physics

ARCHIVES

Neutron-Deuteron Breakup and Quasielastic Scattering

by

Alice Elisabeth Ohlson

Submitted to the Department of Physics
on May 8, 2009, in partial fulfillment of the
requirements for the degree of
Bachelor of Science in Physics

Abstract

Quasielastic scattering and deuteron breakup in the 200 MeV region is studied by impinging a pulsed neutron beam on a deuterium target at the Weapons Neutron Research facility at the Los Alamos Neutron Science Center. The scattered neutrons from the $d(n,np)n$ reaction are detected by a wall of neutron time-of-flight scintillators, and scattered protons are detected by two scintillators and a wire chamber. This setup allows for measurement of the incident neutron energy, scattered neutron energy, and scattered proton energy, as well as the scattering angle and position of the scattered neutron. The results of the experiment are compared with a Monte Carlo simulation of neutron-proton scattering, to observe the differences between two-body and three-body quasielastic collisions. The four-dimensional differential cross section for the $d(n,np)n$ reaction is determined from the data.

Thesis Supervisor: June Matthews
Title: Professor of Physics

Acknowledgments

I would like to thank Professor June Matthews for all of the help, advice, and support she has given me in the past two years. Thanks also to Taylan Akdoğan, Michael Kovash, and Steven Wallace for providing me with the tools I needed to complete this thesis. Finally, infinite thanks to my parents; without their love nothing is possible.

Contents

1	Introduction	17
2	Experimental Setup	19
2.1	Neutron Beam Production	19
2.2	Deuterium Target	21
2.3	Fission Chamber	21
2.4	Proton Detection	21
2.5	Neutron Detection	24
2.6	Detector Geometry	25
3	Calibrations	29
3.1	Fission Chamber	30
3.2	dE and P1	31
3.3	Neutron Bars	32
3.3.1	Time of Flight	32
3.3.2	Height	35
3.3.3	Cosmic Ray Detection	37
4	Selection of Good Events	43
4.1	Detector Cuts	44
4.2	Kinematic Cuts	45

5	Interaction Cross Section	49
5.1	N_{inc}	50
5.2	N_{obs} , ΔE_p , and ΔE_n	50
5.3	Scattering Centers per Unit Area	50
5.4	Solid Angles	51
	5.4.1 Neutron Bars	52
	5.4.2 Magnets and P1	52
5.5	Detector Efficiencies	54
6	Monte Carlo Simulation	55
6.1	Coordinate System	56
6.2	User Inputs	56
6.3	Event Generation	57
	6.3.1 “At-Rest” Particle Momentum	59
6.4	Neutron-Proton Elastic Scattering	59
6.5	Neutron Bar Location	61
6.6	Physical Constraints	61
6.7	Example Simulation	62
6.8	Realistic Simulation	63
7	Results	69
7.1	$E_{in} = 100MeV$	71
7.2	$E_{in} = 200MeV$	72
7.3	$E_{in} = 300MeV$	74
7.4	Error Analysis	75
8	Conclusions	87

List of Figures

2-1	Flight paths at WNR. Neutron beams from Target 4 are marked in blue. The neutron deuteron breakup experiment used flight path 4FP15R, marked “ND Breakup,” and detectors were located in building 29A, shown in red.[4]	20
2-2	Fission chamber ADC spectrum. The left peak corresponds to alpha particles and the right peak to fission fragments.	22
2-3	Experimental setup, to scale.	23
2-4	The geometry of the P1 detector and the rear magnet, and the definition of angles. All distances are in centimeters.	26
2-5	The geometry of the neutron bars and definition of angles. The top image is a top-down view of the beam-left setup. The bottom image defines the widths of the neutron bars. All distances are in centimeters. The bars are numbered 0 to 8 from left to right (inside bar to outside bar).	27
3-1	Incident neutron kinetic energy spectrum from fission chamber. The γ -flash is visible in the first few bins.	31
3-2	TOF sum spectra for each neutron bar, showing two possible γ -flash candidates. (The bars are numbered 0 through 8, left-to-right, top-to-bottom.)	33
3-3	TDC difference spectra.	35

3-4	Cutting the TDC difference spectrum on events that triggered NC0.	36
3-5	Calibration of neutron bar heights.	37
3-6	Neutron bar height spectra after calibration. The hairline gaps in the spectra are due to binning.	39
3-7	Six cosmic ray tracks are plotted in the left graph. The right graph shows only the five whose linear fits have R^2 values greater than 0.75. The horizontal axis is the horizontal location of the hit along the neutron wall (determined by which bar was hit; each bar is 10cm wide) and the vertical axis is the height of the event on the neutron bar (both axes in centimeters).	40
3-8	The calibrations in Table 3.3 give these spectra for each neutron bar when the differences between the fit and the actual data points are calculated. The horizontal axis is the height of the event, and the vertical axis is the difference between the actual event location and the location predicted by the linear fit (both axes in centimeters).	41
3-9	Adjusting the calibrations from Figure 3-8 yields these spectra.	41
3-10	Histogram of the slopes of the cosmic ray tracks.	42
4-1	The number of events as a function of number of neutron bars recording a signal.	45
4-2	Cleaning up the TOF vs. ADC spectrum.	46
4-3	Cutting on the TOF vs. ADC spectrum cleaned up this graph of energy vs. ADC as well.	47
4-4	Top: When the incident energy is cut around 200MeV, a clear peak is seen in the scattered neutron energy spectrum corresponding to quasielastic scattering. Bottom: The background events are cut out.	48
5-1	Geometry of the magnets. All lengths are in centimeters.	53

6-1	Definition of angles and lengths in the Monte Carlo simulation.	58
6-2	The energy of the incoming neutron and the (cylindrical) interaction area in the example simulation.	63
6-3	Energy and momenta of the “at rest” proton in the example simulation.	64
6-4	Energy and detection location of the ejected proton in the example simulation.	64
6-5	Energy, detection location, and bin number of the outgoing neutron in the example simulation.	65
6-6	The energy of the incoming neutron and the (cylindrical) interaction area in the realistic simulation.	65
6-7	Energy and momenta of the “at rest” proton in the realistic simulation.	66
6-8	Energy and detection location of the ejected proton in the realistic simulation.	66
6-9	Energy, detection location, and bin number of the outgoing neutron in the realistic simulation.	67
7-1	The velocities (divided by c) of the incident neutron(top), scattered proton (middle) and scattered neutron (bottom).	70
7-2	The energies of the incident neutron(top), scattered proton (middle) and scattered neutron (bottom).	71
7-3	The energy of the incident neutron (horizontal axis) plotted against the energy of the scattered proton (vertical axis), for all scattered neutron energies.	72
7-4	The energy of the incident neutron (horizontal axis) plotted against the energy of the scattered neutron (vertical axis), for all scattered proton energies.	73
7-5	The number of events recorded by each neutron bar.	74

7-6	The velocities (divided by c) of the incident neutron (top), scattered proton (middle) and scattered neutron (bottom), when the data are cut around 100MeV.	75
7-7	The energies of the incident neutron (top), scattered proton (middle) and scattered neutron (bottom), when the data are cut around 100MeV.	76
7-8	The number of events recorded by each neutron bar, when the data are cut around 100MeV.	77
7-9	The interaction cross section, $\frac{d^4\sigma(E_{in}=100MeV)}{dE_p dE_n d\Omega_p d\Omega_n}$ in mb/sr ² /MeV ²	78
7-10	The velocities (divided by c) of the incident neutron (top), scattered proton (middle) and scattered neutron (bottom), when the data are cut around 200MeV.	79
7-11	The energies of the incident neutron (top), scattered proton (middle) and scattered neutron (bottom), when the data are cut around 200MeV.	79
7-12	The number of events recorded by each neutron bar, when the data are cut around 200MeV.	80
7-13	The interaction cross section, $\frac{d^4\sigma(E_{in}=200MeV)}{dE_p dE_n d\Omega_p d\Omega_n}$ in mb/sr ² /MeV ²	80
7-14	The interaction cross section, $\frac{d^3\sigma(E_{in}=200MeV)}{dE_p d\Omega_p d\Omega_n}$ at $\theta_n = 55^\circ$ and $\theta_p = 25^\circ$.	81
7-15	The interaction cross section, $\frac{d^3\sigma(E_{in}=200MeV)}{dE_p d\Omega_p d\Omega_n}$ at $\theta_n = 55^\circ$ and $\theta_p = 35^\circ$, in mb/sr ² /MeV, from [7].	81
7-16	The interaction cross section, $\frac{d^3\sigma(E_{in}=200MeV)}{dE_p d\Omega_p d\Omega_n}$ at $\theta_n = 55^\circ$ and $\theta_p = 45^\circ$, in mb/sr ² /MeV, from [7].	82
7-17	The velocities (divided by c) of the incident neutron (top), scattered proton (middle) and scattered neutron (bottom), when the data are cut around 300MeV.	82
7-18	The energies of the incident neutron (top), scattered proton (middle) and scattered neutron (bottom), when the data are cut around 300MeV.	83

7-19	The number of events recorded by each neutron bar, when the data are cut around 300MeV.	83
7-20	The interaction cross section, $\frac{d^4\sigma(E_{in}=300MeV)}{dE_p dE_n d\Omega_p d\Omega_n}$ in mb/sr ² /MeV ²	84
7-21	The error in energy, σ_T , as a function of total energy, E . Here t is allowed to vary, but ℓ is fixed. (The errors are plotted for kinetic energies between 0 and 800 MeV.	85

List of Tables

2.1	Dimensions and locations of the proton detectors.	25
2.2	Angles subtended by proton detectors.	25
2.3	Angles of neutron wall.	26
2.4	Angles subtended by individual neutron bars.	27
3.1	Calibrations for the dE and P1 detectors.	32
3.2	The neutron bar TOF calibrations.	34
3.3	The neutron bar height calibrations calculated with the NC detectors and the bar edges.	38
5.1	Properties of the fission chamber and of ^{238}U	50
5.2	Properties of liquid deuterium and of the target.	51
5.3	The solid angles of the neutron bars.	52
5.4	Magnet geometry from Figure 5-1.	53

Chapter 1

Introduction

Investigating the interactions between protons and neutrons, collectively known as nucleons, is fundamental to the study of nuclear physics. While two-nucleon collisions have been analyzed theoretically and experimentally to a high degree of accuracy, extending two-nucleon theoretical models to three particles yields predictions which disagree with experimental data. These discrepancies indicate the presence of a physical process that is not yet understood, generally named the three-nucleon force. There is a need for further experimental and theoretical work in the area of three-nucleon interactions.

The simplest system with three nucleons that can be studied is one nucleon colliding with a bound proton and neutron. Most such experiments have consisted of a proton colliding with a deuteron (the nucleus of a deuterium atom), as in [7], for example. The experiment described and analyzed here instead features a neutron colliding with a deuteron. While the resolution and statistics in this experiment are not high enough to be able to detect the effects of the three-nucleon force, the lessons learned from this analysis will hopefully be useful in future similar experiments that are able to probe deeper into nuclear interactions.

Chapter 2

Experimental Setup

In this experiment, neutron-induced breakup of deuterons is studied by detecting two of the resulting free nucleons: the proton and one of the two neutrons. Data were collected at the Weapons Neutron Research (WNR) facility at the Los Alamos Neutron Science Center (LANSCE) at the Los Alamos National Laboratory. The neutron source at WNR provides the incident neutrons (Section 2.1), and detectors on one side of the beamline detect and measure the energy of the scattered proton (Section 2.4). A wall of scintillator bars on the other side of the beamline detects the scattered neutron (Section 2.5).

2.1 Neutron Beam Production

The linear accelerator at LANSCE produces a pulsed proton beam which is directed into several targets and experimental areas. At WNR the proton beam impinges on a spallation tungsten source (Target 4), producing neutrons with energies ranging continuously up to 800MeV. The neutrons are collimated into several beams that are directed at different experimental setups. The neutrons are delivered in 40 635 μ s-long macropulses per second. Each macropulse is made up of 200ps micropulses, separated

by $1.8\mu\text{s}$.

A map of the WNR flight paths is shown in Figure 2-1. The neutron-deuteron breakup experiment is located 15° to the right of the proton beam, on flight path 4FP15R, in the building marked 29A.[2]

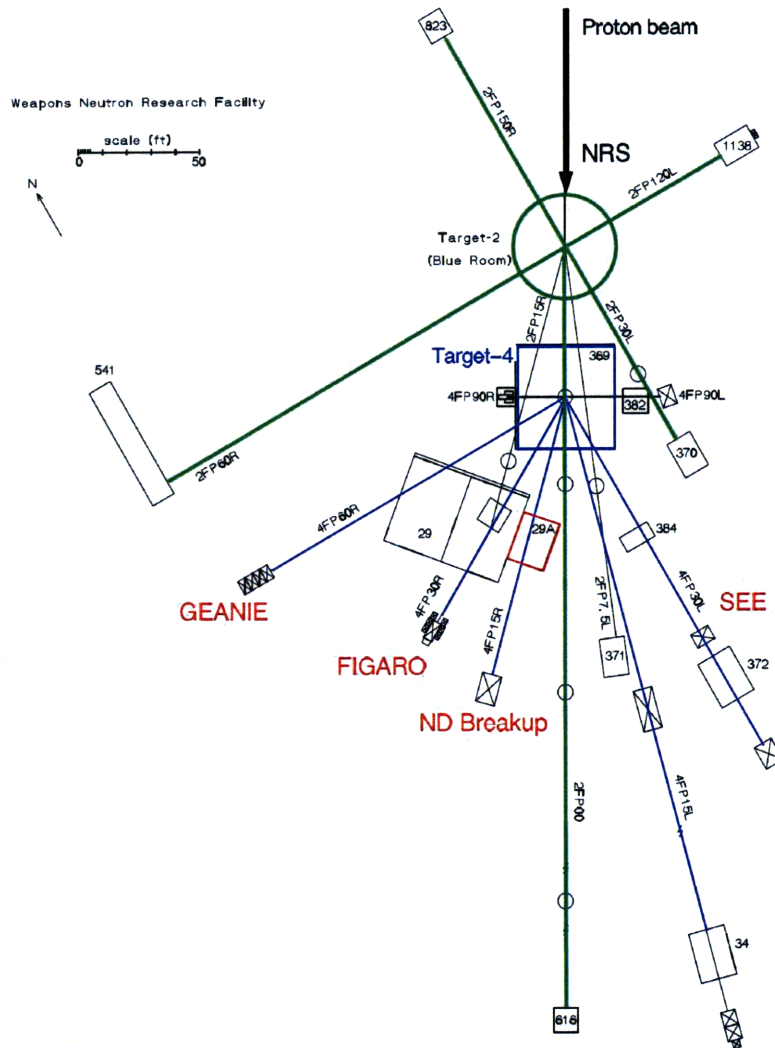


Figure 2-1: Flight paths at WNR. Neutron beams from Target 4 are marked in blue. The neutron deuteron breakup experiment used flight path 4FP15R, marked “ND Breakup,” and detectors were located in building 29A, shown in red.[4]

2.2 Deuterium Target

In this experiment the neutron beam was incident upon a target of liquid deuterium (2H), although some data were collected with a liquid hydrogen (H_2) target and an empty target for calibration purposes. The liquid deuterium filled a cylindrical container with a diameter of 3" (7.6cm). The container consisted of a 0.002"-thick mylar cylindrical surface and 6.5mm-thick steel top and bottom surfaces. The cylinder was oriented vertically, so that the neutron beam passed through the cylindrical surface, in order to eliminate scattering from the steel covers. The target was housed inside a cylindrical scattering chamber with a diameter of 32cm.[4]

2.3 Fission Chamber

The flux of incident neutrons as a function of energy is measured with a fission chamber located upstream of the deuterium target. The chamber contains several thin foils of ^{238}U . As a neutron passes through the layers of uranium it can cause fission resulting in two heavy fission fragments plus neutrons and alpha particles (4He). Two pieces of information are known about these fission fragments: the time-of-flight of the neutron that caused the ^{238}U to fission and the ADC pulse height. The ADC information is important for distinguishing between alpha particles and fission fragments (Figure 2-2). The background alpha particles detected are discarded, and the times-of-flight corresponding to the fission fragments are used to determine the neutron beam energy spectrum.[2]

2.4 Proton Detection

There were several detectors on the proton side of the experiment, although not all of them were used in this analysis. The experimental setup is shown in Figure 2-3.

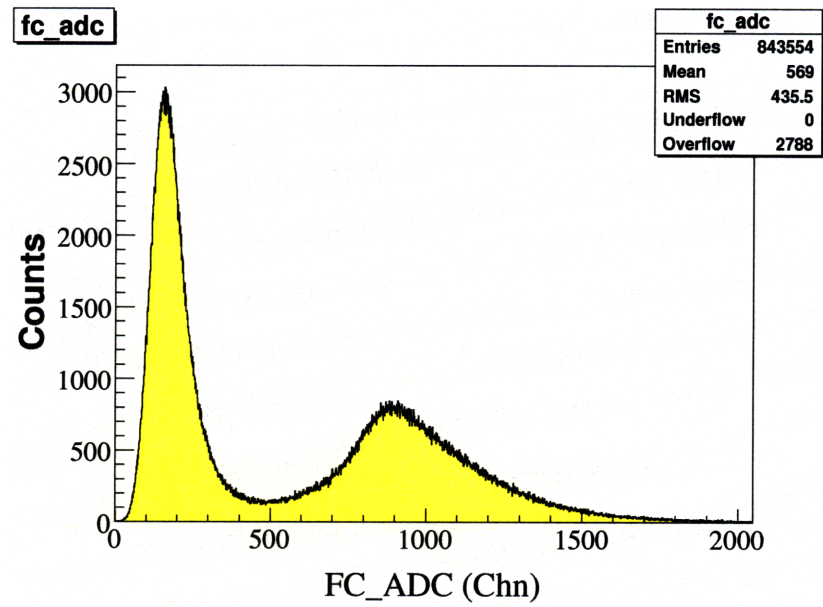


Figure 2-2: Fission chamber ADC spectrum. The left peak corresponds to alpha particles and the right peak to fission fragments.

Not shown are an additional set of neutron bars behind the P1 and P2 detectors, and the upstream fission chamber.

If an incident neutron scatters from the proton in the deuterium nucleus, the recoiling proton can be knocked out of the target, and can encounter a thin plastic scintillator known as the ΔE , or dE, detector. As a charged particle passes through the scintillator it interacts via the Coulomb interaction with the medium surrounding its track. As the excited molecules return to their ground state, scintillation light is emitted. This light is collected in a photomultiplier tube, where it produces photoelectrons which are then multiplied, producing a measureable signal. The electronic pulse produced by the amplified photoelectron current is the indication that a charged particle has passed through the detector. Plastic scintillators have fast response times and high light output [6], allowing the time-of-flight to the dE detector to be determined to within 1ns. Since this detector is at a far forward angle and is close to the deuterium target, the detected protons are carrying most of the energy of the inci-

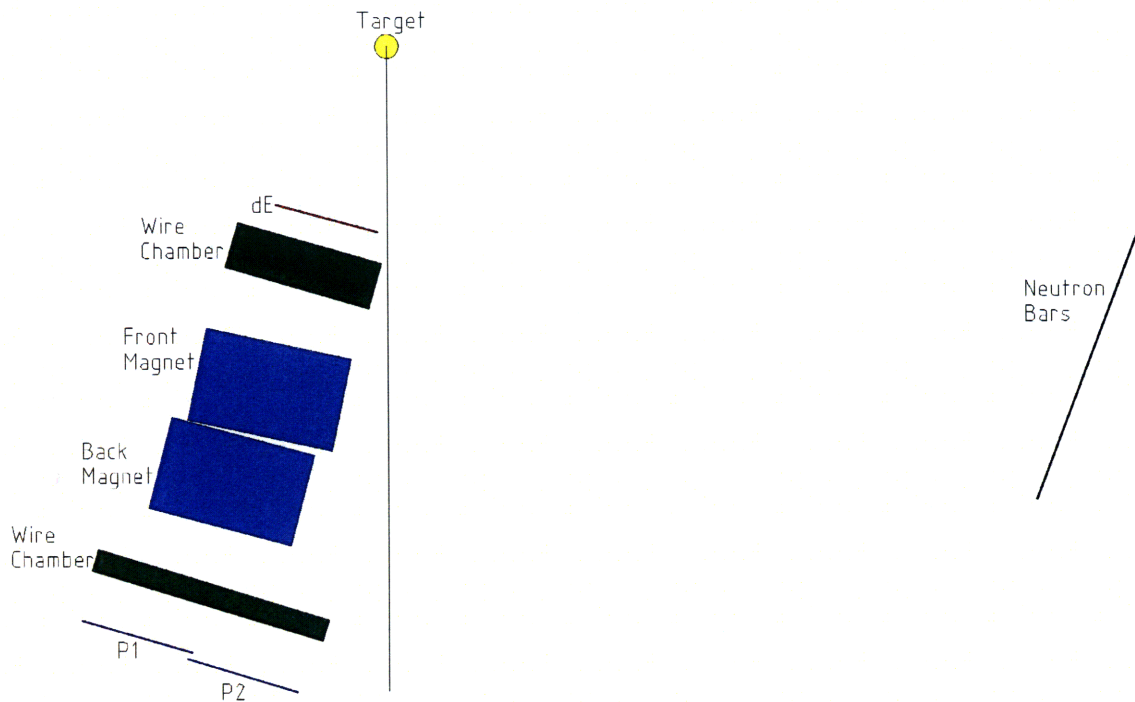


Figure 2-3: Experimental setup, to scale.

dent neutrons. Therefore the measurement of the time-of-flight to the dE detector was used to calculate the incident neutron energy on an event-by-event basis.

The second detector on the proton side was a wire chamber. The wire chamber consists of four parallel planes of wires, two with the wires oriented horizontally and two with vertical wires. The planes are immersed in a gas mixture of 69% argon and 31% isobutane. When a charged particle passes through the wire chamber it ionizes the argon, and the charged ions drift towards the nearby wires, creating an electrical pulse upon reaching a wire. By knowing which wires were struck, the position of the ionization event can be determined in the horizontal and vertical directions. Unfortunately, although protons passing through the chamber could be detected, the

electronics were not working well enough to obtain good position resolution, so this detector was only used to eliminate random coincidences.

The proton then passes through two magnets and a second wire chamber. Had the wire chamber electronics been working well, the wire chamber-magnet combination would have been used to determine the proton momentum, by calculating the radius of curvature of the proton's path through the magnetic field through precise position measurements. However, due to resolution limitations, the proton's momentum was determined through time of flight measurements instead. The magnets and second wire chamber were not used except to limit the solid angle subtended by the proton detection system.

The proton is finally detected by either the P1 or the P2 scintillator. The time-of-flight difference between the dE and P1 detectors was used to measure the energy of the scattered proton. The P2 detector was not working correctly, so only P1 was used in the final analysis.

This experiment was only looking for coincidences between neutrons (on beam left) and protons (on beam right), so the beam right neutron bars were unused.

2.5 Neutron Detection

Neutrons are detected using bars of plastic scintillator located on beam left. While neutrons are uncharged and therefore cannot directly excite the molecules in the scintillator, they do scatter off the hydrogen and carbon nuclei. The recoiling protons from these elastic collisions can be detected in the plastic scintillator as described in Section 2.4. The times-of-flight to the neutron bars were used to calculate the scattered neutron energy, and the geometry of the neutron bars determined the neutron scattering angle.

2.6 Detector Geometry

The information given about the geometry of the detectors were measured distances between the detectors and the target and beamline. From these distances the acceptance angles of all detectors were calculated using the Law of Cosines. The width of each detector ($L1$) and the distances to the inside and outside edges of the detector ($L2$ and $L3$), along the beamline ($L4$), and between the beamline and detector ($L5$), were provided for each proton detector and the neutron wall. These measurements are given in Table 2.1, and Figure 2-4 shows these distances for the P1 detector. The angles from the inner edge of the detector to the beamline (f), and between the inner and outer edges (g), for the scintillators and wire chambers were calculated and are shown in Table 2.2.

Table 2.1: Dimensions and locations of the proton detectors.

Detector	$L1(\text{cm})$	$L2(\text{cm})$	$L3(\text{cm})$	$L4(\text{cm})$	$L5(\text{cm})$
dE	34.5	59.2	61.9	59.8	3.1
Wire Chamber 1	48.8	69.5	74.2	67.6	2.7
Wire Chamber 2	78.7	183.9	185.9	183.0	19.4
P1	37.5	203.4	208.2	196.9	64.2
P2	37.5	207.7	205.6	208.9	29.9

Table 2.2: Angles subtended by proton detectors.

Detector	f	g
dE	2.929°	33.008°
Wire Chamber 1	1.604°	39.534°
Wire Chamber 2	6.055°	24.567°
P1	18.365°	10.369°
P2	8.225°	10.395°

The same calculations were done for the wall of neutron bars. The distances are

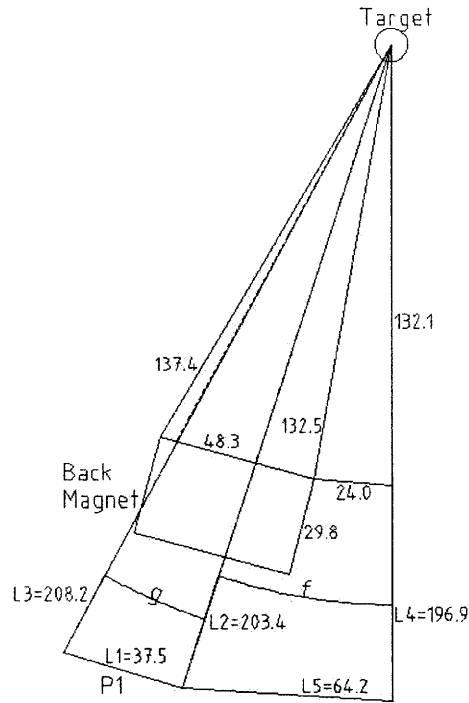


Figure 2-4: The geometry of the P1 detector and the rear magnet, and the definition of angles. All distances are in centimeters.

shown in Figure 2-5, and the angles a , b , and c were calculated from these distances (Table 2.3). By knowing these angles and the widths of each neutron bar, the angle to each bar (d), the angle subtended by each bar (e), and the distance to each bar (L) can be calculated. These values are shown in Table 2.4. The horizontal acceptance of each bar was from d to $d + e$.

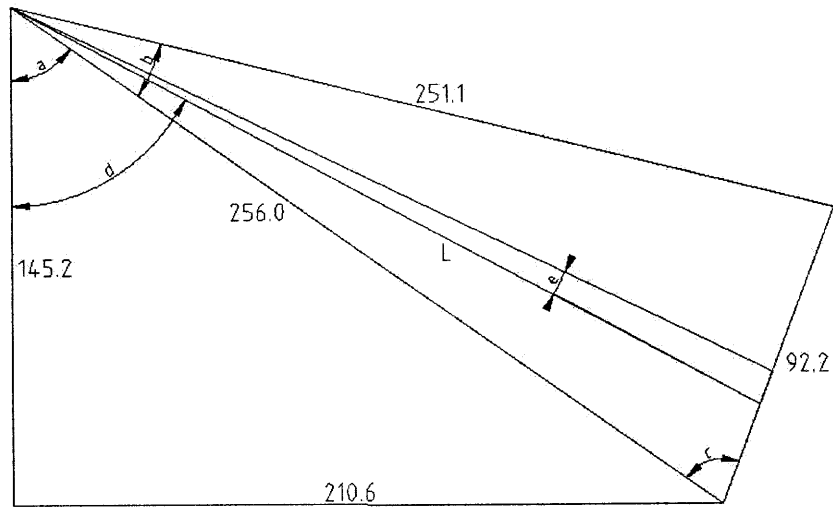
Table 2.3: Angles of neutron wall.

a	0.966^r	55.35°
b	0.365^r	20.92°
c	1.336^r	76.54°

The geometry of the magnets will be discussed in Section 5.4.2.

Table 2.4: Angles subtended by individual neutron bars.

<i>Bar#</i>	<i>d</i>	<i>e</i>	<i>L</i>
0	55.35°	2.31°	256.0 cm
1	57.66°	2.28°	253.8 cm
2	59.93°	2.35°	252.0 cm
3	62.28°	2.33°	250.6 cm
4	64.61°	2.36°	249.6 cm
5	66.97°	2.35°	249.1 cm
6	69.32°	2.32°	249.0 cm
7	71.64°	2.36°	249.3 cm
8	74.00°	2.27°	250.0 cm



10.5	10.2	10.4	10.2	10.3	10.2	10.1	10.3	10.0
------	------	------	------	------	------	------	------	------

Figure 2-5: The geometry of the neutron bars and definition of angles. The top image is a top-down view of the beam-left setup. The bottom image defines the widths of the neutron bars. All distances are in centimeters. The bars are numbered 0 to 8 from left to right (inside bar to outside bar).

Chapter 3

Calibrations

The detectors used in this experiment record an “event” with two pieces of information: ADC (analog to digital converter) and TDC (time to digital converter) signals. The ADC converts analog information from the detector, such as the amount of energy lost as a particle passes through (which is determined by the light collected in the photomultiplier tube), into a digital signal that can be read out with electronics. Precise calibrations of the ADC spectra obtained in this experiment were not necessary, it is enough to know that they are correlated with the energy of the particle.

The TDC converts the time between two signals (the t_0 pulse and the event) into a digital readout. The t_0 pulse is produced whenever a proton bunch hits the spallation target, and is delivered electronically to all the experimental setups at WNR, in order to be used as a reference for all TDC signals.[2] Since much of the analysis for this experiment was based on time-of-flight (TOF) measurements, it was necessary to calibrate the TDC spectra carefully. Generally, time is linearly related to the TDC channel.

$$\text{time} = a\text{TDC} + b \tag{3.1}$$

In Equation 3.1, a and b are constants. These factors, one additive and one

multiplicative, must be calculated for the TDC spectrum of each detector. The following sections will deal primarily with calculating these constants. Note that the actual time-of-flight of any particle is given by

$$\text{TOF} = a\text{TDC} + b - \text{TOF}_{t_0} \quad (3.2)$$

3.1 Fission Chamber

The time spectrum of the fission chamber was calibrated by using two events with known times-of-flight. When a pulse hits the tungsten target, photons are produced along with neutrons. Traveling at the speed of light, they reach the detectors before the neutrons, creating an easily-identifiable “ γ -flash.” The time corresponding to this early, sharp peak can be calculated since the path length from the target to the detector is known.

A second feature of the TDC spectrum that can be correlated with a specific time value is a low-energy process that occurs at 6.66 MeV.[2] The timing associated with this peak is given by

$$t = \frac{\ell}{c\sqrt{1 - \left(1 + \frac{6.66\text{MeV}}{m_p c^2}\right)^{-2}}} \quad (3.3)$$

The distance from the tungsten target to the fission chamber (ℓ) was 1545.0cm. Therefore the γ -flash should occur at time 52ns, and the low energy process should be around 435ns. A Gaussian fit to the fission chamber TDC spectrum shows that these two events occurred at TDC values of 1196 and 156.5, respectively. The calibration is therefore $a = -0.369$ and $b = 492.838$. The velocity of the neutrons can be calculated from the TOF and ℓ , and the kinetic energy (T) can then be calculated using Equation 3.4. After calibration, the fission chamber energy spectrum looks as shown in Figure 3-1.

$$T = \frac{mc^2}{\sqrt{1 - v^2/c^2}} - mc^2 = \frac{mc^2}{\sqrt{1 - (\ell/TOF)^2/c^2}} - mc^2 \quad (3.4)$$

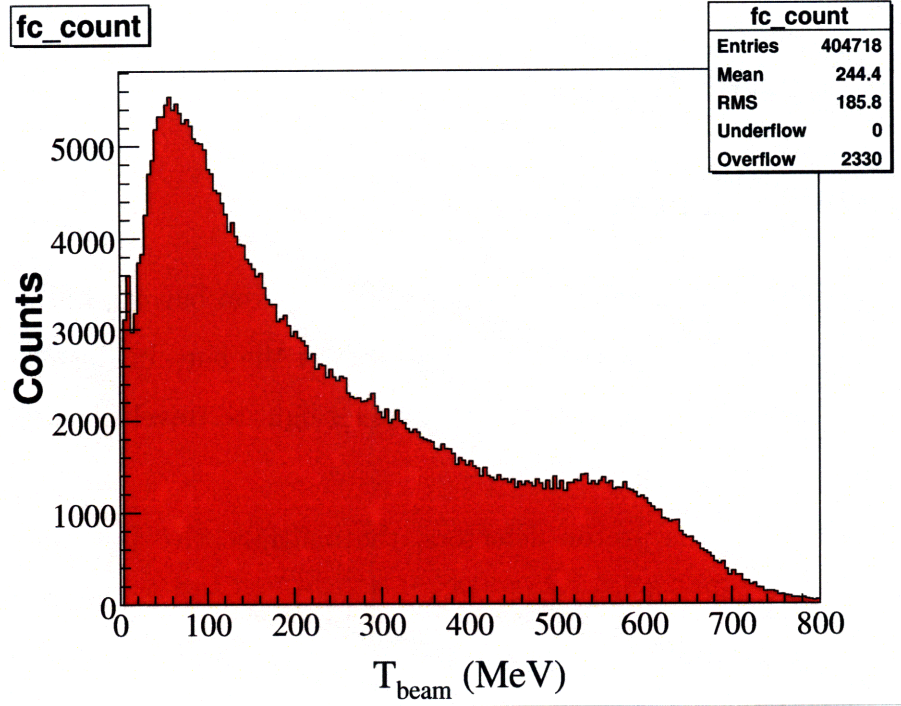


Figure 3-1: Incident neutron kinetic energy spectrum from fission chamber. The γ -flash is visible in the first few bins.

3.2 dE and P1

The scintillators used for proton detection were also calibrated using the γ -flash, which determined the additive conversion constant. The multiplicative conversion factor of time per TDC channel was previously determined by feeding pulses with known frequency into the electronics. The calibration factors are listed in Table 3.1

Table 3.1: Calibrations for the dE and P1 detectors.

Detector	a	b
dE	0.1429360	237.186
P1	0.1388139	263.843

3.3 Neutron Bars

3.3.1 Time of Flight

The time-of-flight of the scattered neutron to the neutron bar is a linear function of half the sum of the TOFs to the top and bottom of the bar. In this linear function the additive constant includes the time it takes for light to travel from one end of the neutron bar to the other.[5]

As in the case of the proton detectors, the multiplicative factors for the TDC calibration of the neutron bars had already been measured. The task remaining was to determine the additive constant. Locating the γ -flash for every detector (18 total: one at the top and the bottom of each bar) individually proved elusive in this case, which can be due to thresholds on the TDCs set incorrectly (particularly on the bottom detectors) and also to small numbers of photons being scattered at large angles. However, it was only necessary to calibrate the sums of the TOFs to the tops and bottoms of each bar. When looking at the TOF sum spectra (shown in Figure 3-2), though, it was noticed that there are actually two peaks which are candidates for the γ -flash.

The “real” γ -flash was picked out by calculating the hypothetical TOFs (and thus the neutron energy) corresponding to each peak for one neutron bar (Bar 0). Originally, the first peak was located in bin 63, the second peak in bin 91, and the leading edge of the neutron spectrum was around bin 102. Because the distance from the target to Bar 0 is 1950cm, the γ -flash is expected to arrive in 65ns. If the

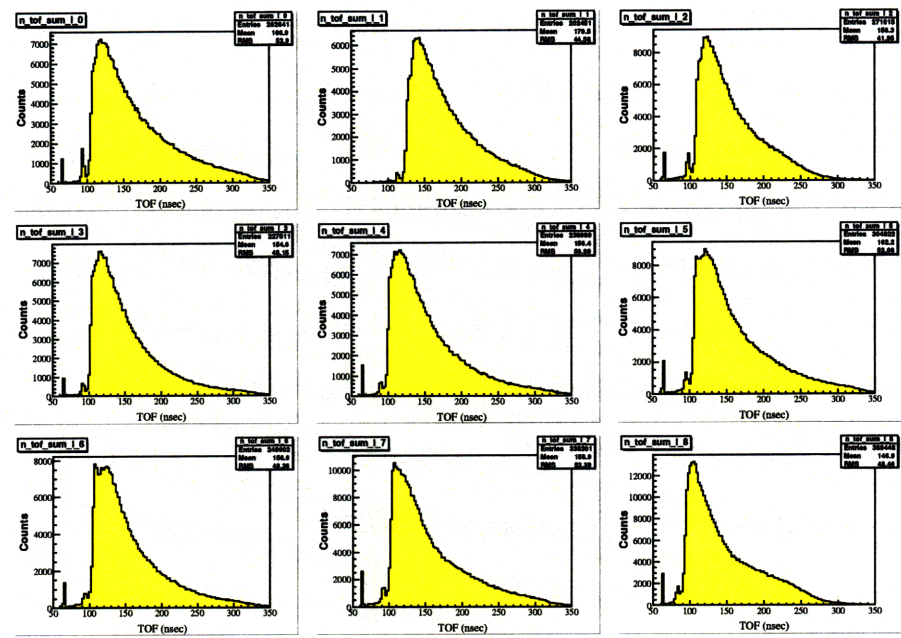


Figure 3-2: TOF sum spectra for each neutron bar, showing two possible γ -flash candidates. (The bars are numbered 0 through 8, left-to-right, top-to-bottom.)

first peak corresponds to 65ns, then the fastest neutrons have a TOF of 104ns. This corresponds to a kinetic energy of 264MeV. Conversely, if the second peak is the real γ -flash, then the fastest neutrons have a TOF of 76ns and a kinetic energy of 872MeV. The maximum energy of the protons incident on the spallation target is 800MeV, and so this high neutron kinetic energy is not possible.

There is even more striking evidence to rule out the second peak. When the data were cut so that the incident neutron energy was below 400MeV, the first bin of neutrons shifted to 107. If the first peak was the γ -flash, then the maximum neutron energy would be 230MeV, which is sensible. If the second peak was the γ -flash, then the maximum scattered neutron kinetic energy would be 635MeV. This large energy discrepancy leads to the conclusion that the first peak in the TOF spectrum is the γ -flash. Consequently the TOF sum spectra were calibrated according to the timing of the first peak.

Locating the γ -flash did not solve all the difficulties in calibrating the neutron

bars. In Figure 3-2 it seems that Bar 1 does not have a visible γ -flash at all. This is due to the threshold on the TDCs being set too high for both top and bottom detectors. In order to solve this problem, the TOF of the leading edge of the neutron spectrum was calculated for every bar. A linear regression was applied to these times, and the TOF of the leading edge of the neutron spectrum for Bar 1 was interpolated from this line. Although the TOFs are not linear as a function of bar number (nor should they be), the variations were small enough so that a linear fit gave a rough calibration for Bar 1.

The final neutron TOF calibrations are shown in Table 3.2.

Table 3.2: The neutron bar TOF calibrations.

Bar #	a	b
0T	0.1285292	302.14
0B	0.1288038	302.14
1T	0.1236540	280.70
1B	0.1284430	280.70
2T	0.1288425	299.52
2B	0.1293234	299.52
3T	0.1297517	301.52
3B	0.1289497	301.52
4T	0.1284508	301.64
4B	0.1300247	301.64
5T	0.1281702	299.84
5B	0.1290522	299.84
6T	0.1300143	295.18
6B	0.1307371	295.18
7T	0.1283379	294.98
7B	0.1295789	294.98
8T	0.1310966	295.33
8B	0.1308894	295.33

3.3.2 Height

The position where the particle strikes the vertical neutron detectors (the “height” where the event takes place) is linearly related to the difference between the times-of-flight to the top of the bar and to the bottom of the bar.[5] Therefore it is also linearly related to the difference in TDC channels recorded by the detectors at the top and bottom of the bar. The quantity $1/2(TDC_{\text{bottom}} - TDC_{\text{top}})$ is calculated for every event and the results are plotted in histograms, known as the TDC difference spectra (shown in Figure 3-3). There are two ways to find a and b from these spectra and thus calibrate the neutron bar height measurements.

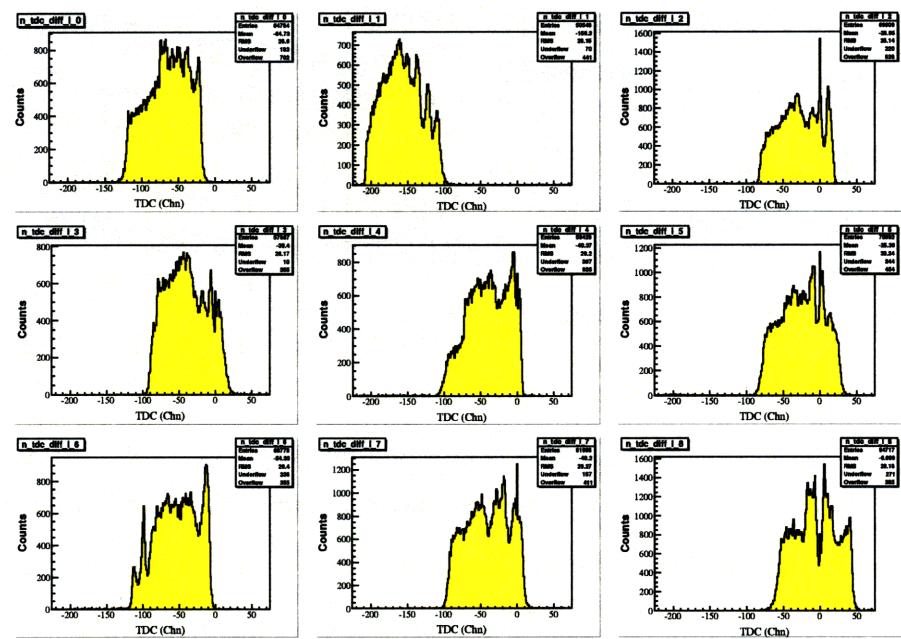


Figure 3-3: TDC difference spectra.

The first method uses the two beam left “neutron calibration” (NC) detectors, which are horizontal scintillators placed at known heights behind the neutron bars. When plotting only events that hit both a neutron bar and a particular NC detector, sharp peaks appear in the time difference spectra (Figure 3-4), and those time differences correspond to the height of the NC detector. NC0 is located at 80cm from the

floor and NC1 is located at 185cm from the floor. The presence of two NC detectors allows two heights to be known, and two points define a line allowing a and b to be found.

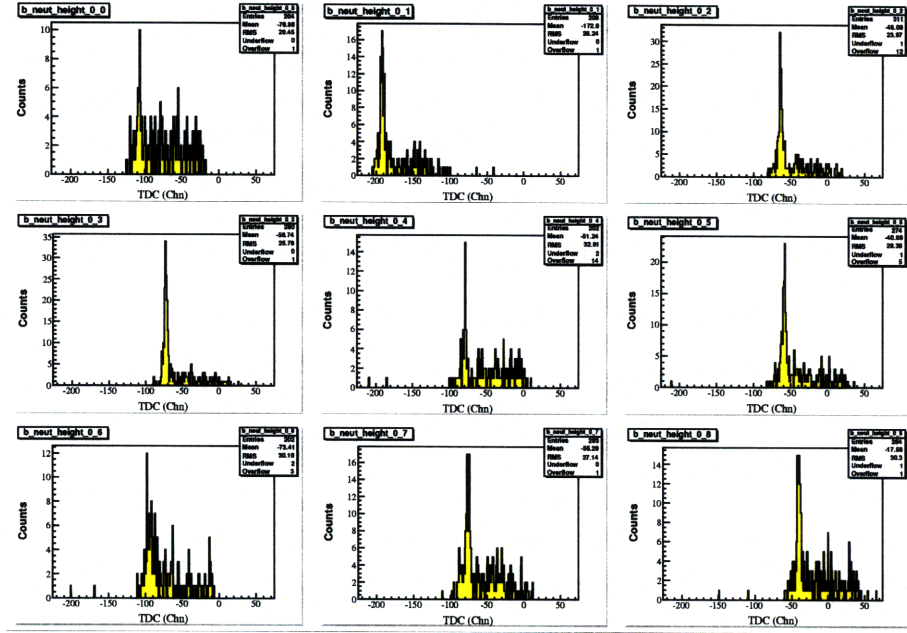


Figure 3-4: Cutting the TDC difference spectrum on events that triggered NC0.

A second method relies on the observation that the time difference spectra drop off sharply on each end. If those drop-offs are assumed to be the edges of the neutron bar, then another two points are defined. One can pick a certain cut-off, such as where the number of events drops below 1000, and use that cutoff to define the edges of the bar. Knowing that the bars are 2m in length allows another two points to be used for calibration (the bar edges are taken to be 51cm and 251cm from the floor).

ROOT was used to fit all four points found in the above manners to a straight line (Figure 3-5). This mitigates the effects of misplaced peaks in the NC spectra, and erroneous bar edge measurements due to spread out time difference spectra.

The fit results are used to convert the time difference $1/2(TOF_{\text{bottom}} - TOF_{\text{top}})$ to the height where the neutron impacted the bar. The calibration constants calcu-

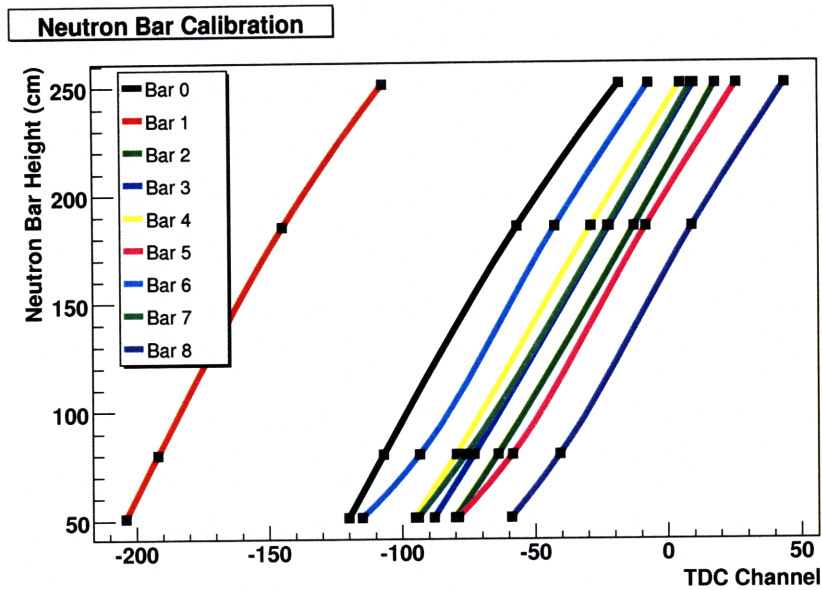


Figure 3-5: Calibration of neutron bar heights.

lated in this way are shown in Table 3.3. After calibration, the neutron height spectra look like those shown in Figure 3-6.

3.3.3 Cosmic Ray Detection

When the neutron beam is off (in the times between macropulses) cosmic rays cause events to be recorded by the neutron bars. Analyzing their spectra can be an interesting exercise and even lead to improved neutron bar calibrations. When 7 or more bars are triggered within a short time span while the neutron beam is off, then the event is likely a cosmic ray. If the cosmic ray is travelling in the plane of the bars, then the tracks can be seen by plotting the heights of each neutron bar hit.

Sometimes the cosmic ray hits will not form a line. If multiple particles happen to be travelling perpendicular to the bars, then they can trigger a cosmic ray event but a track will not be visible. Or sometimes a track will form through 6 bars, but the 7th is caused by a different particle coming within a small time frame. Sometimes tracks will even look oscillatory, which may be due to two cosmic rays passing through

Table 3.3: The neutron bar height calibrations calculated with the NC detectors and the bar edges.

Bar #	a	b
0	1.972	290.476
1	2.075	477.829
2	2.046	212.650
3	2.046	230.186
4	2.015	241.752
5	1.943	199.915
6	1.895	263.889
7	1.952	231.323
8	1.977	164.679

the bars at different heights, since the tops of the oscillations form a track as do the bottoms. By doing a linear fit to each track and eliminating events with an R^2 value less than 0.75, the “good” cosmic ray events can be isolated (see Figure 3-7). (R^2 is the “coefficient of determination,” where $R^2 = 0$ means the data exhibit no linear trend, and $R^2 = 1$ means the data are perfectly linear.)

Plotting the difference of the measured value and the value predicted by the linear fit can be used for fine tuning neutron height calibrations. For example, if the measured height on Bar 2 is consistently lower than the predicted value then b can be increased for Bar 2. Before any “fine tuning” has occurred, 3,000 events give the time difference spectra shown in Figure 3-8.

It is obvious from Figure 3-8 that the value a is too low for Bars 1 and 8, and too high for Bars 2 and 4. It also appears that b is too high for Bar 0. After adjusting the necessary values, the same spectra are shown in Figure 3-9. Although cosmic ray tracks were not used for calibration during the final analysis here, this shows one method that can be used for refining measurements in the future.

It is interesting to note the similarities between Figure 3-9 and the neutron height spectra in Figure 3-6. If the bars are evenly illuminated by neutrons, then the neutron

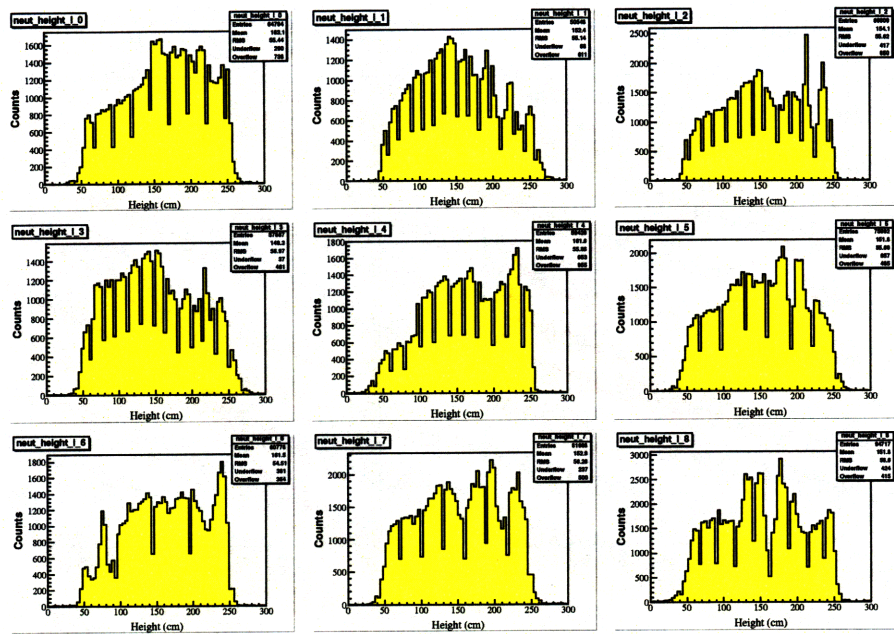


Figure 3-6: Neutron bar height spectra after calibration. The hairline gaps in the spectra are due to binning.

height spectra should be flat; if the cosmic ray tracks are straight then the spectra in Figure 3-9 should be flat also. Where the neutron height spectra deviate from uniformity, so too do the cosmic ray fit spectra. This indicates that the peaks and valleys in Figure 3-6 are not due to the bars failing to trigger on events at certain heights, but rather that events at certain heights are being interpreted electronically as being too high or too low, as evidenced from Figure 3-9.

The slopes of the cosmic ray linear fits are recorded in a histogram in Figure 3-10. These data make intuitive sense: There is a dip in the middle because relatively few cosmic rays are travelling horizontally as seen from any point on Earth. (Additionally, the restriction on R^2 can cut out lines with low slopes, even if the fit is relatively good.) The drop-off towards higher slopes is also expected because the size of the bars defines a finite acceptance angle for cosmic rays to trigger 7 or more bars. The maximum expected slope is in the case of the particle hitting the very top of the first bar and hitting the very bottom of the seventh bar. This would yield a slope of 200cm/70cm or

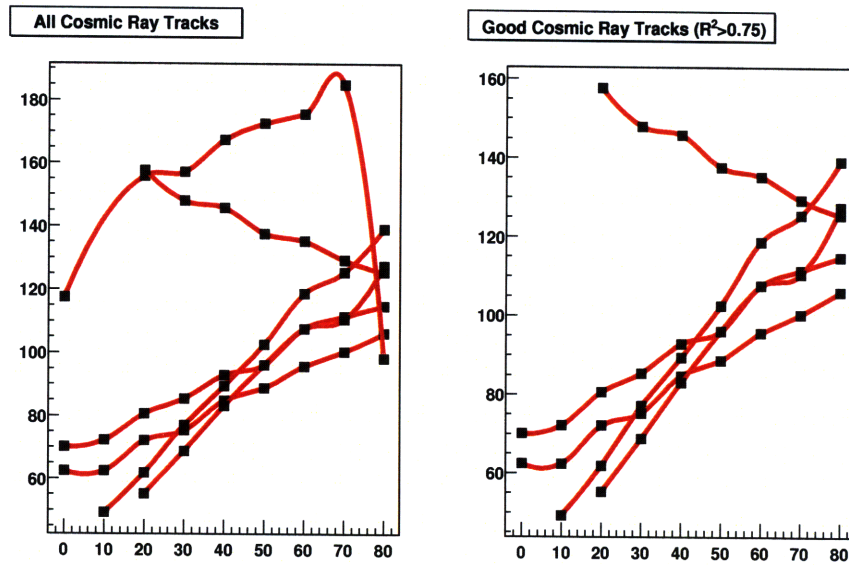


Figure 3-7: Six cosmic ray tracks are plotted in the left graph. The right graph shows only the five whose linear fits have R^2 values greater than 0.75. The horizontal axis is the horizontal location of the hit along the neutron wall (determined by which bar was hit; each bar is 10cm wide) and the vertical axis is the height of the event on the neutron bar (both axes in centimeters).

2.86. This is consistent with the cut-off seen in Figure 3-10. The expected spectrum is doubly-peaked and centered around zero, trailing off around ± 2.86 . Also, the heights of the two peaks should be about equal, since the cosmic rays are not only coming from one direction. This qualitatively matches the experimentally-obtained spectrum.

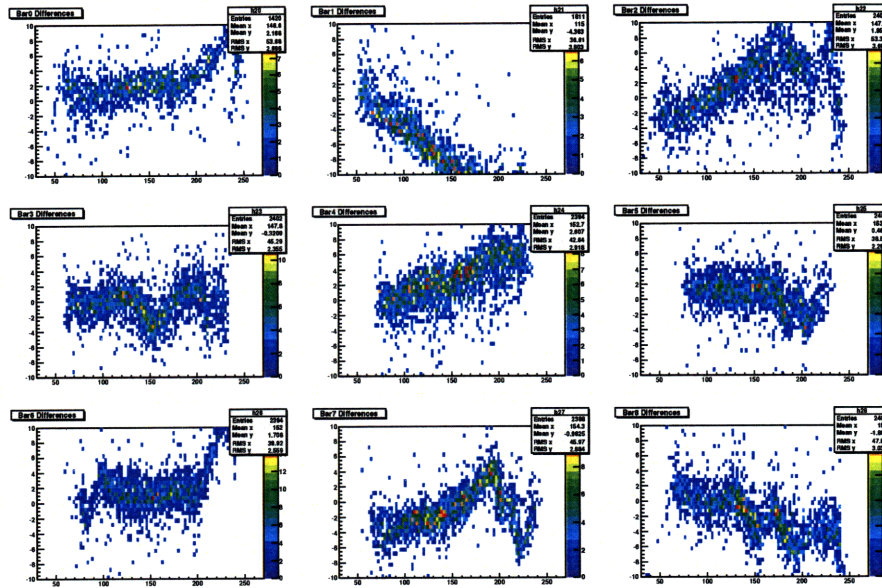


Figure 3-8: The calibrations in Table 3.3 give these spectra for each neutron bar when the differences between the fit and the actual data points are calculated. The horizontal axis is the height of the event, and the vertical axis is the difference between the actual event location and the location predicted by the linear fit (both axes in centimeters).

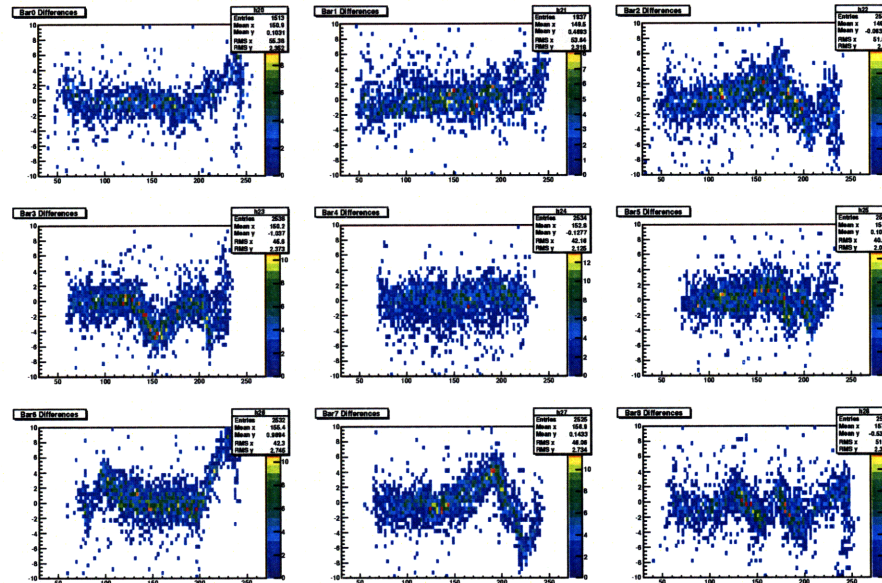


Figure 3-9: Adjusting the calibrations from Figure 3-8 yields these spectra.

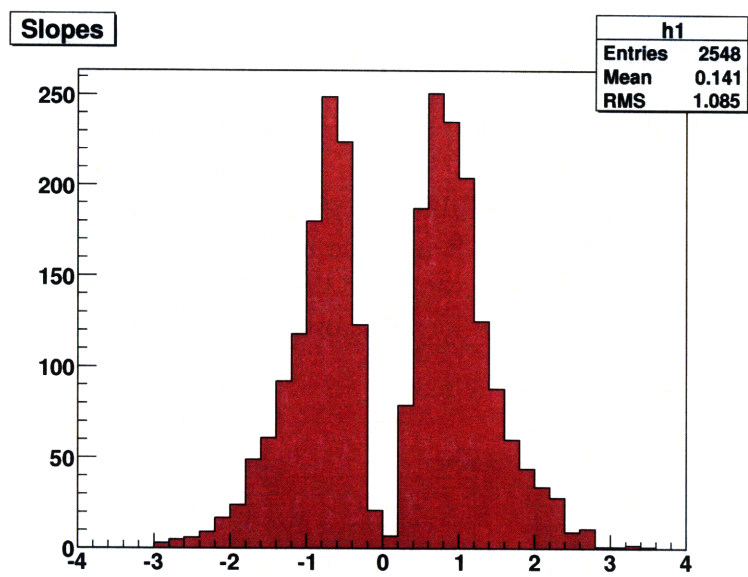


Figure 3-10: Histogram of the slopes of the cosmic ray tracks.

Chapter 4

Selection of Good Events

The events used for analysis of neutron-deuteron scattering must satisfy a series of requirements which verify that they are not only real $d(n,np)n$ events, but also that they contain enough information to be analyzed. The data cuts used to find “good” events were:

1. A t_0 pulse must be present.
2. All four planes in the front wire chamber must record a signal.
3. Exactly one neutron bar must detect a signal.
4. Both the ADC and TDC on the dE detector must record a signal.
5. Both the ADC and TDC on the P1 detector must record a signal.
6. The kinetic energy of the incident neutron must be above 33 MeV.
7. The velocity of the incident neutron must be between 0 and c .
8. The velocity of the scattered proton must be between 0 and c .
9. The velocity of the scattered neutron must be between 0 and c .

10. The detected proton must pass cuts on the ADC versus TOF spectrum.
11. The detected neutron must pass cuts on the energy spectrum.

The data analyzed here were collected in 17 2-hour runs during the summer of 2007. Of the total 5,258,110 events in those 17 runs, only 335,026 passed the cuts for “good” events.

4.1 Detector Cuts

The event that this experiment is meant to record is a neutron breaking up a deuteron such that one of the scattered neutrons is detected in the beam left neutron bars and the proton is detected on beam right. First there must be a t_0 pulse indicating that a proton micropulse has arrived at the spallation target. Many events that occur without a t_0 pulse are background neutrons left in the room from other micropulses. Both the dE and P1 detectors must record ADC and TDC signals. All four of the planes in the front wire chamber must detect an event. The combination of these three detectors allows many background protons to be eliminated. Additionally, exactly one neutron bar must detect an event. Although it is reasonable for an event to be recorded in multiple neutron bars (because a recoil proton scatters into an adjoining bar, for example), the structure of the data analysis code requires that only events striking one bar are permitted. This does not cut out a significant number of events, as shown in Figure 4-1. The coincident detection of particles on both the proton and neutron sides of the experimental apparatus constitutes the np event that we are looking for.

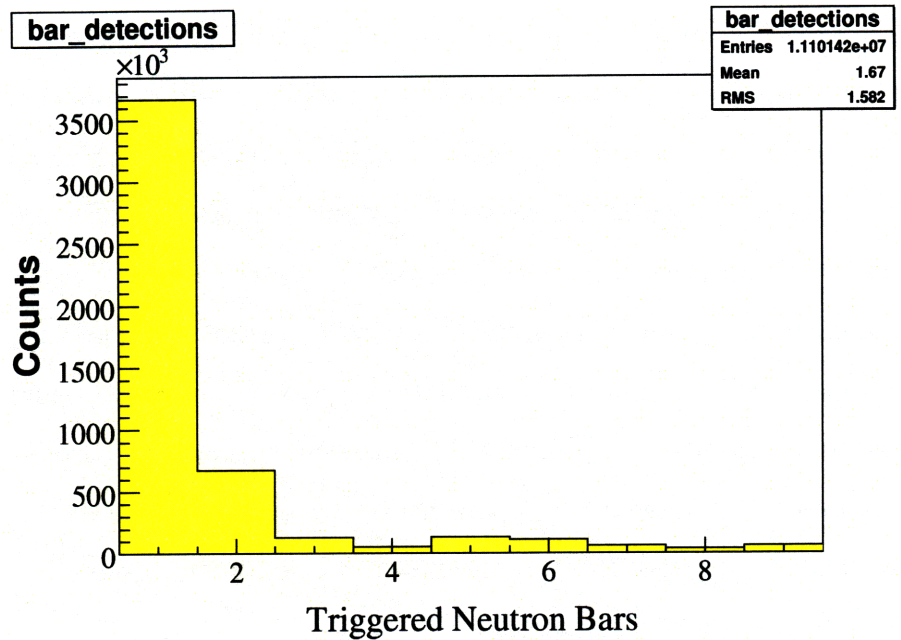


Figure 4-1: The number of events as a function of number of neutron bars recording a signal.

4.2 Kinematic Cuts

In addition to eliminating background by looking for coincident events in several detectors, it is also necessary to determine whether the data collected from those detectors make sense kinematically. The energy of the incident neutron must surpass a threshold for an event to be considered valid. It is possible for very low energy neutrons from previous pulses to be mixed in with neutrons from the current pulse, and their properties are impossible to determine since they appear to be paired with the wrong t_0 pulse. By looking at the data, a threshold of 33 MeV was set; when incident neutron energies below this cut are discarded then the data become much “cleaner.” This is however the minimum threshold that had the desired effect of “cleaning up” the data. This experiment is not concerned with energies that low, and so higher cuts are placed on the incident energy during analysis.

The velocities of the detected particles are calculated, and any events with negative

velocities or velocities greater than the speed of light are not counted.

There are two ways of measuring proton energies in this experiment, through time-of-flight measurements and using ADC data. Although using the ADC values for exact quantitative measurements of energy requires additional calibrations and analysis that did not take place, a correlation between ADC channel and particle energy (obtained from TOF measurements) is still expected. A plot of ADC versus TOF is shown in Figure 4-2. The correlation is easily visible, although there are many background events in which the ADC is not correlated. To eliminate these background events, a Gaussian curve was fit to each ADC channel in the histogram. Any event occurring beyond 2σ from the mean of the Gaussian was discarded. The result is shown in Figures 4-2 and 4-3.

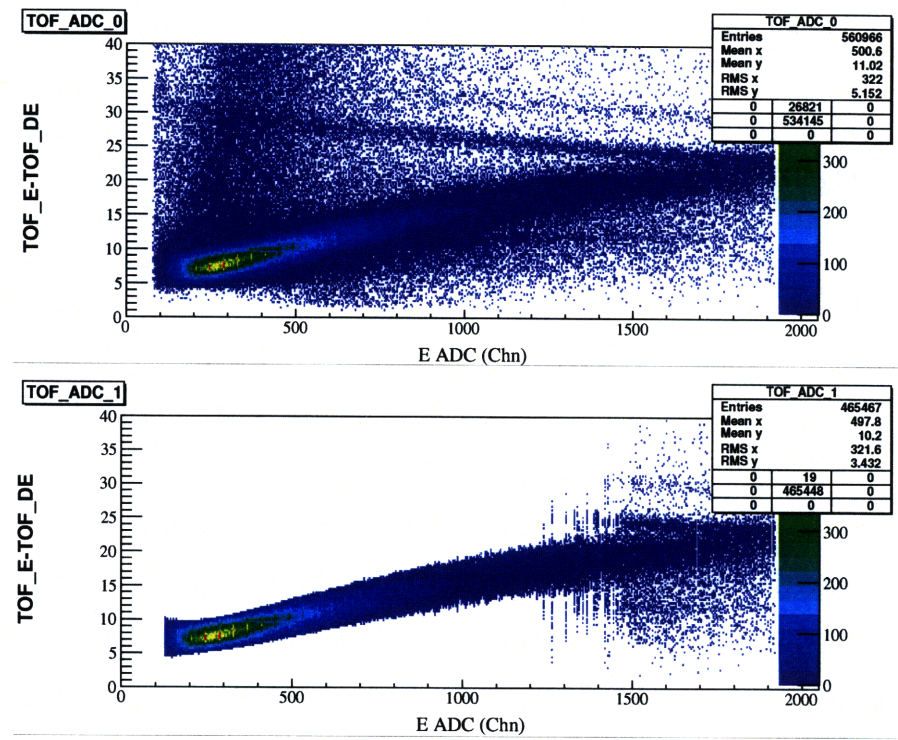


Figure 4-2: Cleaning up the TOF vs. ADC spectrum.

The malfunctioning of the P2 detector was discovered also by using this method. When the same histogram (as Figure 4-2) was plotted for P2 there was no such clear

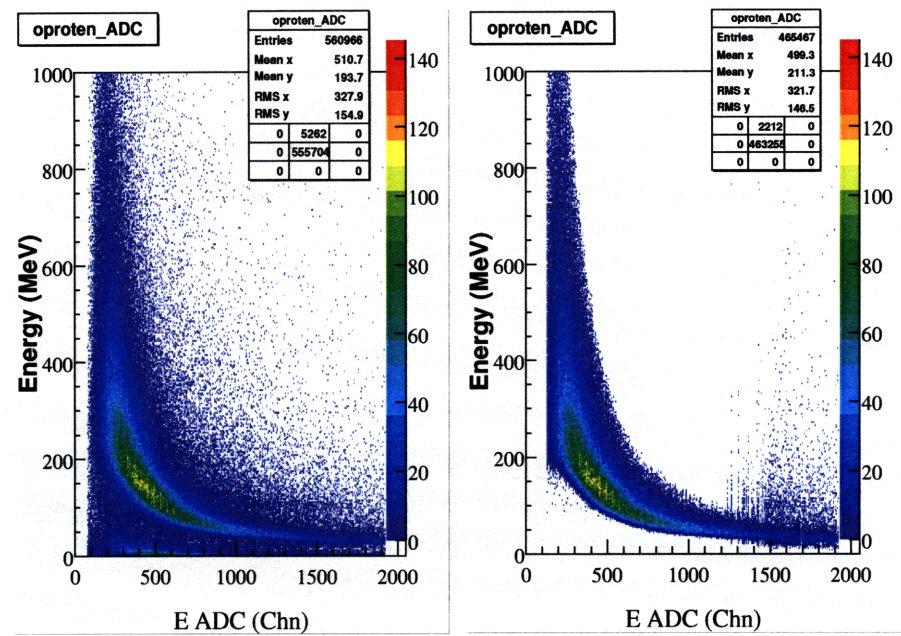


Figure 4-3: Cutting on the TOF vs. ADC spectrum cleaned up this graph of energy vs. ADC as well.

correlation between ADC channel and TOF, and so it was decided to use only the P1 detector in the analysis.

When the incident neutron energy is cut on a certain energy range (as in Chapter 7), there is normally a clear peak in the scattered neutron energy spectrum that corresponds to quasielastic scattering. This peak is superimposed on a background of neutron events that appears independently of the incident neutron energy. In order to eliminate this background, a Gaussian was fit to the quasielastic peak, and events with energies beyond 2σ from the mean of the Gaussian were discarded (Figure 4-4). An improvement over this analysis could be fitting the energy spectrum with a decaying function (for example, exponential or power law) plus a Gaussian, and then discarding the background events described by the decaying function.

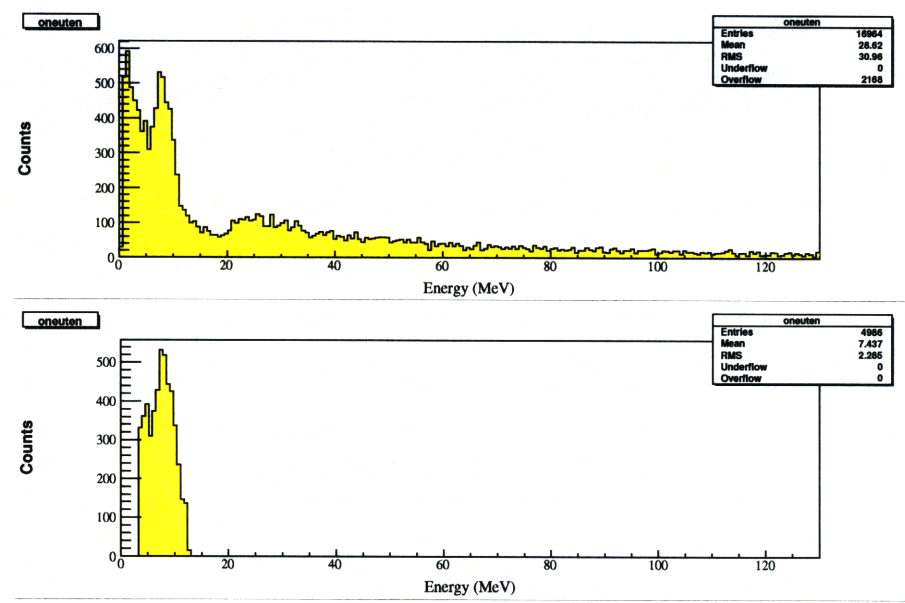


Figure 4-4: Top: When the incident energy is cut around 200MeV, a clear peak is seen in the scattered neutron energy spectrum corresponding to quasielastic scattering. Bottom: The background events are cut out.

Chapter 5

Interaction Cross Section

In this section the four-dimensional differential cross section for the $d(n, np)n$ reaction will be determined as a function of incident neutron energy, with respect to the energies and scattering angles of the neutron and proton.

The cross section is defined as the number of interactions that occur per unit time divided by the number of incident particles per unit time and the scattering centers per unit area for a given incident energy.[1] However, in this experiment, data are not collected over the full 4π spatial sphere nor over all particle energies. Dividing the cross section by the ranges of energies and the ranges of angles accessed in this experiment yields the differential cross section. The cross section is described symbolically in Equation 5.1, where t is the number of scattering centers per unit area, N_{inc} and N_{obs} are the number of incident and observed scattered particles, and ΔE and $\Delta\Omega$ are the energy ranges and solid angles over which the differential cross section is evaluated.

$$\frac{N_{obs}/time}{t * N_{inc}/time} = \frac{d^4\sigma(E_{in})}{d\Omega_p d\Omega_n dE_p dE_n} \Delta\Omega_p \Delta\Omega_n \Delta E_p \Delta E_n \quad (5.1)$$

5.1 N_{inc}

The flux of incident neutrons is calculated from fission chamber data. Counting fission fragments (discussed in Section 2.3) in an energy range around E_{in} yields N_{fis} , which is related to the neutron flux (N_{inc}) by the efficiency of the chamber (ϵ), the cross section of ^{238}U (σ_U) and the density of ^{238}U in the chamber (ρ_U).

$$N_{inc} = \frac{N_{fis}(E)}{\epsilon \rho_U \sigma_U(E)} \quad (5.2)$$

Table 5.1: Properties of the fission chamber and of ^{238}U .

ϵ	0.98
σ_U	1.2 barns/atom
ρ_U	0.9080×10^{-6} atoms/barn

These quantities were measured in [2] and are reported in Table 5.1. The final relation between fission fragments detected and neutron flux is $N_{inc} = 9.4 \times 10^5 N_{fis}$.

5.2 N_{obs} , ΔE_p , and ΔE_n

The number of observed interactions is the number of coincidences that pass all the cuts on “good” events (discussed in Chapter 4) in certain ranges of scattered proton and neutron energies. ΔE_p and ΔE_n describe the widths of those ranges.

5.3 Scattering Centers per Unit Area

The “thickness” t of the target, or the number of scattering centers per unit area, is given by Equation 5.3, where N_A is Avogadro’s number, A is the atomic mass, L is the length of target that the beam travels through, and ρ is the density of liquid

deuterium. Using the values shown in Table 5.2, the thickness was calculated to be $3.85 \times 10^{23} \text{cm}^{-2}$.

$$t = \frac{N_A L \rho}{A} \quad (5.3)$$

Table 5.2: Properties of liquid deuterium and of the target.

N_A	6.022×10^{23} atoms/mole
A	2.014 g/mole
L	7.62 cm
ρ	0.169 g/cm^3

5.4 Solid Angles

The definition of solid angle, with respect to a center point O (in this experiment, the position of the target), is the surface integral given in Equation 5.4.

$$\Omega = \iint \frac{\hat{n} \cdot dA}{r^2} \quad (5.4)$$

For a plane, the solid angle depends on the distance z , defined as the length of a line extended perpendicularly from the plane that passes through O . Then $\hat{n} \cdot dA = dxdy \cos \theta$ where $\cos \theta = z/r$ and $r^2 = x^2 + y^2 + z^2$. x and y are defined as the horizontal and vertical distances along the plane from the point where z intersects the plane. Assuming a point source of particles (instead of the actual extended deuterium target), Equation 5.5 describes the solid angle subtended by any plane.

$$\Omega = \int_{y_1}^{y_2} \int_{x_1}^{x_2} \frac{z dxdy}{(x^2 + y^2 + z^2)^{3/2}} \quad (5.5)$$

5.4.1 Neutron Bars

The solid angles subtended by the detectors were calculated from the detector geometry, discussed in Chapter 2. Referring back to Figure 2-5, the length z must be given by $256 \sin c = 248.97\text{cm}$. The distance that this point occurs from the inside edge of the neutron bars is $256 \cos c = 59.57\text{cm}$, in the middle of Bar 5. Using the known widths of each bar, and the position of the point where z intersects the plane, the limits of integration x_1 and x_2 can be computed.

The beam is 126.5cm above the floor and the neutron bars are 2m tall. The precise heights of the bars above the floor define the limits y_1 and $y_2 = y_1 + 200\text{cm}$. All these quantities, as well as the solid angle of each neutron bar computed from Equation 5.5, are shown in Table 5.3.

Table 5.3: The solid angles of the neutron bars.

<i>Bar#</i>	x_1 (cm)	x_2 (cm)	y_1 (cm)	y_2 (cm)	Ω (sr)
0	-59.57	-49.07	-75.2	124.8	0.0291
1	-49.07	-38.87	-75.7	124.3	0.0289
2	-38.87	-28.47	-75.7	124.3	0.0300
3	-28.47	-18.27	-76.2	123.8	0.0299
4	-18.27	-7.97	-75.8	124.2	0.0304
5	-7.97	2.23	-75.9	124.1	0.0302
6	2.23	12.33	-75.7	124.3	0.0299
7	12.33	22.63	-75.5	124.5	0.0303
8	22.63	32.63	-74.5	125.5	0.0291

5.4.2 Magnets and P1

The magnets and the P1 detector limit the proton-side solid angle.¹ The dimensions of and the distances to the magnets were measured, as well as some of the internal

¹Note that if the wire chambers had been working, the active area of the second chamber would have defined the proton solid angle.

dimensions. The internal magnet geometry is shown in Figure 5-1. Unfortunately, not all dimensions were included. It was necessary to assume that the figure was drawn to scale, and compute the missing measurements from the drawing. The unmarked lengths are labeled in Figure 5-1 and the scaled lengths are listed in Table 5.4.

Table 5.4: Magnet geometry from Figure 5-1.

<i>A</i>	3.16cm
<i>B</i>	3.99cm
<i>C</i>	3.16cm
<i>D</i>	3.91cm

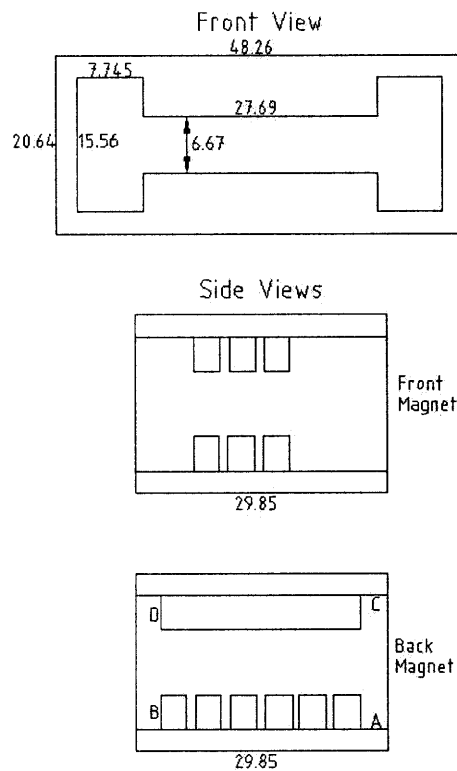


Figure 5-1: Geometry of the magnets. All lengths are in centimeters.

After creating a scale drawing in QCad, it was possible to obtain the angles and distances using that program. The horizontal acceptance of the back magnet was

12.08° to 27.45°. The acceptance of the narrow part of the magnet (the region of the magnetic field) was 14.87° to 24.76°.

Using the same definitions for solid angle quantities as above, the length z must be given by $158.97 \sin 87.16^\circ = 158.77\text{cm}$. The distance that this point occurs from the inside of the magnet is $158.97 \cos 87.16^\circ = 7.88\text{cm}$. However, the P1 detector's acceptance is only for angles 18.365° to 28.734°. The solid angle on the proton side is given by Equation 5.6 and equals 0.00914385.

$$\Omega = \int_{-3.335}^{3.335} \int_{9.56}^{27.55} \frac{(158.97)dx dy}{(x^2 + y^2 + (158.97)^2)^{3/2}} + \int_{-7.78}^{7.78} \int_{27.55}^{35.30} \frac{(158.97)dx dy}{(x^2 + y^2 + (158.97)^2)^{3/2}} \quad (5.6)$$

5.5 Detector Efficiencies

The expression for the four-dimensional differential cross section must be divided by the efficiencies of the detectors, to scale the number of observed coincidence events appropriately. Since charged particles interact very readily with matter, the efficiencies of the dE and P1 detectors were taken to be nearly 100%. The efficiency of the neutron bars, however, was only around 10%, since neutral particles do not interact as often with matter as charged particles.[5]

Chapter 6

Monte Carlo Simulation

When a neutron collides with a deuteron there are three possible outcomes: the neutron can eject the proton from a deuteron elastically, eject the neutron from a deuteron elastically, or interact with both particles in a deuteron via the “three-nucleon force.” This chapter discusses the simulation of neutron-proton quasielastic scattering. While neutron-proton *elastic* scattering can be solved exactly classically and relativistically, in order to apply these results to experimental data there are “real-world” effects that must be taken into account. Some of the effects that will be accounted for in this simulation are:

1. Non-zero kinetic energy of the particles in the deuteron (meaning the scattering is *quasielastic*).
2. Finite beam size and extended target geometry.
3. Physical constraints imposed by the experimental apparatus.

In essence the Monte Carlo simulation works as follows: The user inputs some known quantities, such as those that would be determined by cuts in the experimental data. The simulation randomly generates other quantities for each collision event that would be unknown and unmeasurable to the user. Known lengths are converted

to scattering angles and the system is solved using relativistic equations. The resultant scattering angles are converted back into lengths that are measurable and detectable, to be compared with the experimental data. All of the random quantities are generated many times, producing probability distributions for the results.

6.1 Coordinate System

The following discussion and the Monte-Carlo simulation code use a right-handed coordinate system with \hat{x} along the beam path, \hat{z} pointing vertically down, and \hat{y} in the horizontal plane perpendicular to the beam. θ is the angle in the horizontal plane extending from the x -axis towards the y -axis. ϕ is the angle extending from the z -axis towards the horizontal plane. Beam right corresponds to positive values of θ so that the proton scattering angle is positive, and positive ϕ corresponds to scattering angles below the plane of the experiment.

6.2 User Inputs

The simulation prompts the user for the following quantities:

1. Kinetic energy of the incoming neutrons (E_n) and uncertainty (ΔE_n).

The program picks an energy anywhere in the range $[E_n - \Delta E_n, E_n + \Delta E_n]$ with equal probability, simulating the cuts that will be applied to the data during analysis.

2. Horizontal (w) and vertical (h) positions of the event detection on the first wire chamber and uncertainty (Δw and Δh) in these measurements.

The horizontal position is measured in cm from the edge of the wire chamber closest to the beam line to the edge farthest from the beam line (the value should

lie between 0 and 48.8cm). The vertical position is measured in centimeters from the plane of the beam upwards (positive values) and downwards (negative values). The value of h should be between -16.5cm and 16.5cm . The program picks a detection location anywhere within the box with the corners $(w - \Delta w, h - \Delta h)$ and $(w + \Delta w, h + \Delta h)$ with equal probability.

3. Circular or rectangular beam profile.

When simulating an extended target where the entire beam spot intersects the target (as in the experiment discussed here), then a circular beam profile should be used. If a thin strip target is used, such that events only occur in a thin region in the middle of the beam spot, then a rectangular beam profile is more appropriate.

4. Dimensions of the beam profile.

Depending on the user input in 3, the program prompts for the radius and depth (for a circular beam profile) or the height, width, and depth (for a rectangular beam profile) of the interaction region.

5. Number of events.

The user inputs how many times the simulation will be run. To obtain good probability distributions it is advisable to run more than 10,000 events, but the random number generation in C++ becomes less random if more than about 50,000 events are processed.

6.3 Event Generation

For each event, the energy of the incoming neutron and the exact position where the proton was detected on the wire chamber (w, h) are randomly generated within the bounds given by the user.

The location where the collision occurred is also randomly generated. Because the size of the beam spot on the target is not a one-dimensional point, it cannot be assumed that all events occur at $(0,0,0)$. The location (x,y,z) of the event is generated randomly within the beam spot volume that was set by the user. (The intensity of the neutron beam is nearly uniform and so a constant probability distribution within the beam spot is used.[2]) The angles from (x,y,z) , where the event occurred, to the location where the proton was detected on the wire chamber (parameterized by w and h) were calculated using the following equations.

$$\tan(\theta_p) = \frac{l_1 \sin(\alpha) + w \cos(\epsilon) - y}{l_1 \cos(\alpha) - w \sin(\epsilon) - x} \quad (6.1)$$

$$\tan(\phi_p) = \frac{w \sin(\epsilon) - l_1 \cos(\alpha) + x}{\cos(\theta_p)(h + z)} \quad (6.2)$$

The definitions of the angles α and ϵ , as well as the length l_1 , are shown in Figure 6-1.

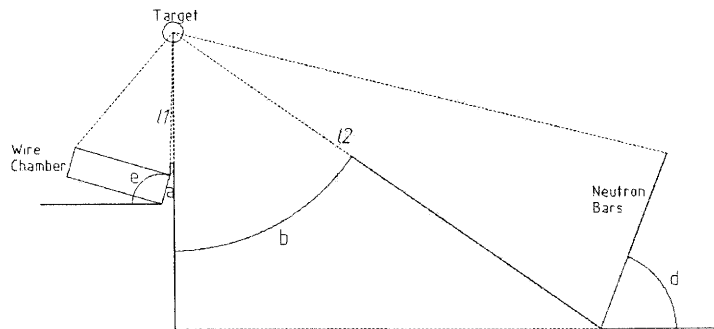


Figure 6-1: Definition of angles and lengths in the Monte Carlo simulation.

Since the “at-rest” nucleons in the deuteron do not really have zero kinetic energy, their momenta were also randomly generated.

6.3.1 “At-Rest” Particle Momentum

The momentum distributions of the neutron and proton inside the deuteron were measured in a study of the $(e, e'p)$ process by Bernheim *et al.* in [3]. Because Gaussian probability distributions are one of the few distributions that are able to be generated randomly (see [8]), the data in [3] was fit by a Gaussian curve ($\sigma = 29.7\text{MeV}/c$). In the Monte Carlo simulation, the momentum of the proton in each of the three directions was randomly assigned according to this Gaussian probability distribution.

6.4 Neutron-Proton Elastic Scattering

Elastic scattering of neutron and protons can be solved exactly using classical or relativistic kinematics, using conservation of energy and momentum. The energies in this experiment require relativistic calculations.

The following notation will be used throughout: Unprimed values represent kinematic quantities before the collision and primed values represent the same quantities after the collision. Energies, momenta, and angles corresponding to the neutron are marked by the subscript n . Likewise, energies, momenta, and angles of the proton are denoted by the subscript p . As the incident neutron only has momentum in the x-direction (the beam is collimated) prior to the collision, it is represented as p_n . The “at rest” proton has momentum in all three directions which are labeled by p_x , p_y , and p_z (note that the subscript p has been dropped with no loss in clarity). The angles θ and ϕ represent post-collision quantities although they are written as unprimed.

Conservation of energy gives:

$$E_n + E_p = E'_n + E'_p \tag{6.3}$$

Conservation of momentum yields three equations:

$$p_n + p_x = p'_n \cos(\theta_n) \sin(\phi_n) + p'_p \cos(\theta_p) \sin(\phi_p) \quad (6.4)$$

$$p_y = p'_n \sin(\theta_n) \sin(\phi_n) + p'_p \sin(\theta_p) \sin(\phi_p) \quad (6.5)$$

$$p_z = p'_n \cos(\phi_n) + p'_p \cos(\phi_p) \quad (6.6)$$

Energy and momentum are related relativistically:

$$E^2 = (pc)^2 + (mc^2)^2 \quad (6.7)$$

where c is the speed of light and mc^2 is the rest energy of the particle.

The detection location of the ejected proton (given by w and h) is known, and therefore θ_p and ϕ_p are known (determined in Equations 6.1 and 6.2). The energy of the incoming beam of neutrons is also known (giving E_n and p_n). The momentum of the “at-rest” proton in the deuteron is randomly generated (discussed in Section 6.3.1). These known quantities will be used to solve for the unknown values: E'_p , p'_p , E'_n , p'_n , θ_n , and ϕ_n .

Solving for the unknowns yields:

$$\text{qty1} = (p_n c + p_x c) \cos(\theta_p) \sin(\phi_p) + p_y c \sin(\theta_p) \sin(\phi_p) + p_z c \cos(\phi_p)$$

$$\text{qty2} = (m_p c^2)^2 - p_n p_x c^2 + E_n E_p$$

$$a = (\text{qty1})^2 - (E_n + E_p)^2$$

$$b = 2(E_n + E_p)(\text{qty2})$$

$$c = -(\text{qty2})^2 - (m_p c^2)^2 (\text{qty1})^2$$

$$E'_p = \frac{-b - \sqrt{b^2 - 4ac}}{2a} \quad (6.8)$$

$$E'_n = E_n + E_p - E'_p \quad (6.9)$$

$$\cos(\phi_n) = \frac{p_z - p'_p \cos(\phi_p)}{p'_n} \quad (6.10)$$

$$\cos(\theta_n) = \frac{p_n + p_x - p'_p \cos(\theta_p) \sin(\phi_p)}{p'_n \sin(\phi_n)} \quad (6.11)$$

6.5 Neutron Bar Location

By using the calculated θ_n and ϕ_n and the known measurements of the beam left neutron bars, the position where the neutron hits a neutron bar can be calculated. The horizontal position along the bar is g (such that Bar 0 starts at $g = 0$ and Bar 8 ends at $g = 92.2$ and the vertical position is l .

$$g = \frac{l_2 \cos(\beta) \tan(\theta_n) - l_2 \sin(\beta) - x \tan(\theta_n) + y}{\sin(\delta) \tan(\theta_n) - \cos(\delta)} \quad (6.12)$$

$$l = -z - \frac{l_2 \cos(\beta) - g \sin(\delta) - x}{\cos(\theta_n) \tan(\phi_n)} \quad (6.13)$$

The definitions of the angles β and δ , as well as the length l_2 , are shown in Figure 6-1.

In addition to displaying the distribution of neutrons across the wall of neutron bars, the neutrons are also sorted into bars to be compared with experimental data.

6.6 Physical Constraints

The principal constraint on the range of proton angles (θ_p and ϕ_p) is the position of the magnets and the P1 detector. Using Equations 6.1 and 6.2, and solving for w and h , the analogous position where the proton hits the back magnet (w_m, h_m) and the P1 detector (w_{P1}, h_{P1}) can be calculated. These formulas are listed in Equation 6.14. The proton hits the P1 detector if $0 < w_{P1} < 37.5$ and $-18.75 < h_{P1} < 18.75$. The

proton passes through the magnet if it passes through one of the following regions:

1. $0 < w_m < 7.745$ and $-7.78 < h_m < 7.78$
2. $7.745 < w_m < 35.435$ and $-3.335 < h_m < 3.335$
3. $35.435 < w_m < 43.18$ and $-7.78 < h_m < 7.78$

$$\begin{aligned}
 w_m &= \frac{158.97 \tan(\theta_p) \cos(12.08^\circ) - x \tan(\theta_p) - 158.97 \sin(12.08^\circ) + y}{\cos(14.92^\circ) + \tan(\theta_p) \sin(14.92^\circ)} \\
 h_m &= \frac{w_m \sin(14.92^\circ) - 158.97 \cos(12.08^\circ) + x - \tan(\phi_p) \cos(\theta_p) z}{\cos(\theta_p) \tan(\phi_p)} \\
 w_{P1} &= \frac{203.4 \tan(\theta_p) \cos(18.36^\circ) - x \tan(\theta_p) - 203.4 \sin(18.36^\circ) + y}{\cos(16.22^\circ) + \tan(\theta_p) \sin(16.22^\circ)} \\
 h_{P1} &= \frac{w_{P1} \sin(16.22^\circ) - 203.4 \cos(18.36^\circ) + x - \tan(\phi_p) \cos(\theta_p) z}{\cos(\theta_p) \tan(\phi_p)}
 \end{aligned} \tag{6.14}$$

6.7 Example Simulation

An example simulation was run for the following user inputs: $E_n = 200 \pm 10\text{MeV}$, $w = 20 \pm 1\text{cm}$ and $h = 1 \pm 1\text{cm}$. A circular beam profile was chosen, with a radius of 1cm and a depth of 7.6cm (3"). 20,000 events were generated. The results of the simulation are shown in Figures 6-2 through 6-5.

This simulation makes it apparent that the solid angle subtended by the back magnet and P1 is very restrictive. Out of 20,000 events, only 1,683 hit P1. Figure 6-2 shows that events from the rear side of the deuterium target are unable to pass through the desired point on the wire chamber and still hit P1, due to angular constraints. Figure 6-3 shows that "at-rest" protons with too much momentum in the $-\hat{x}$ -direction cannot travel at the desired angle either. Figures 6-4 and 6-5 indicate that the assumption that the proton carries almost all of the incident neutron's energy is a good one. The incident energy in this simulation was around 200MeV, and the proton carried away around 175MeV.

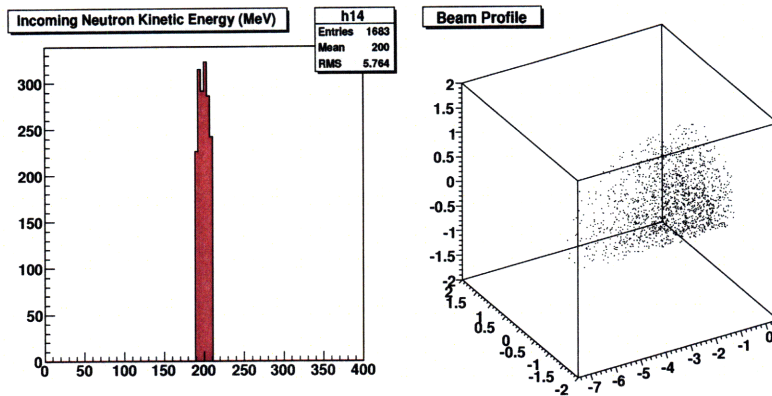


Figure 6-2: The energy of the incoming neutron and the (cylindrical) interaction area in the example simulation.

6.8 Realistic Simulation

Since the wire chamber did not have good enough resolution to cut on events in such a small area, the simulated data will have a better correspondance with the experiment if the uncertainty in wire chamber measurements is expanded such that the proton's position on the wire chamber is randomly distributed over the entire chamber. If this is done, then the shadow of the magnet/P1 acceptance is clearly seen in Figure 6-7, since only protons passing through that area on the wire chamber can pass through the magnet.

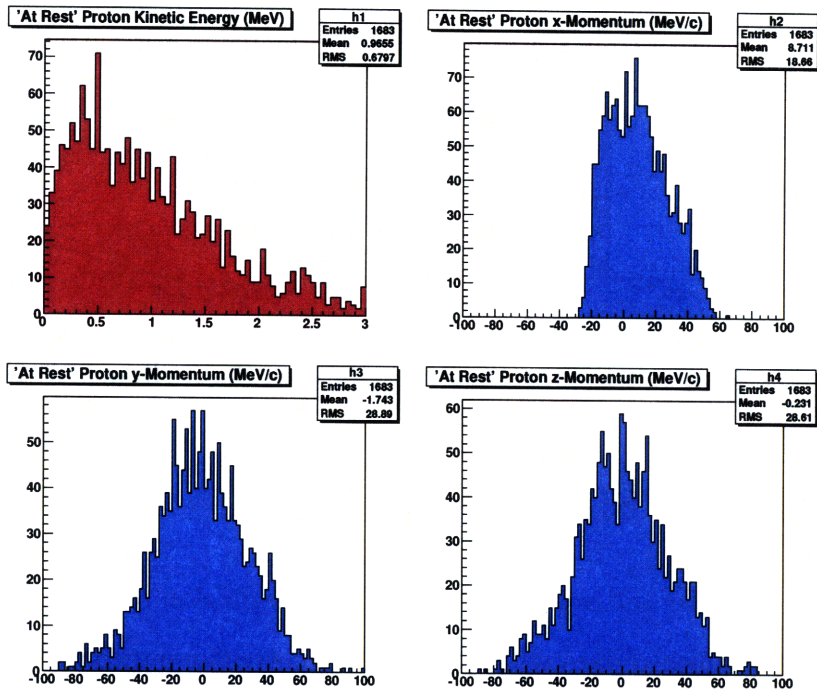


Figure 6-3: Energy and momenta of the "at rest" proton in the example simulation.

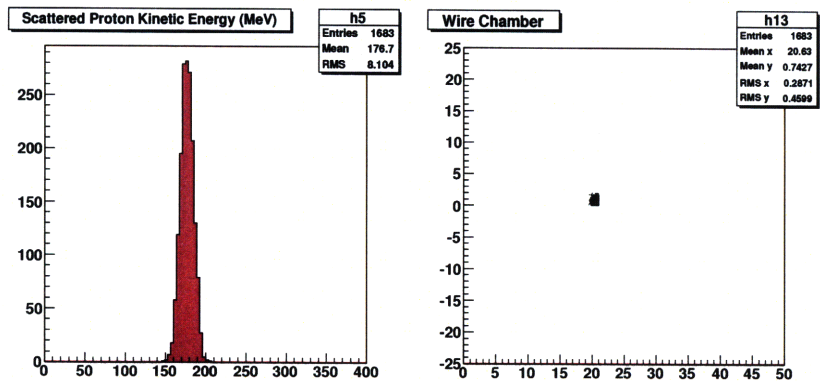


Figure 6-4: Energy and detection location of the ejected proton in the example simulation.

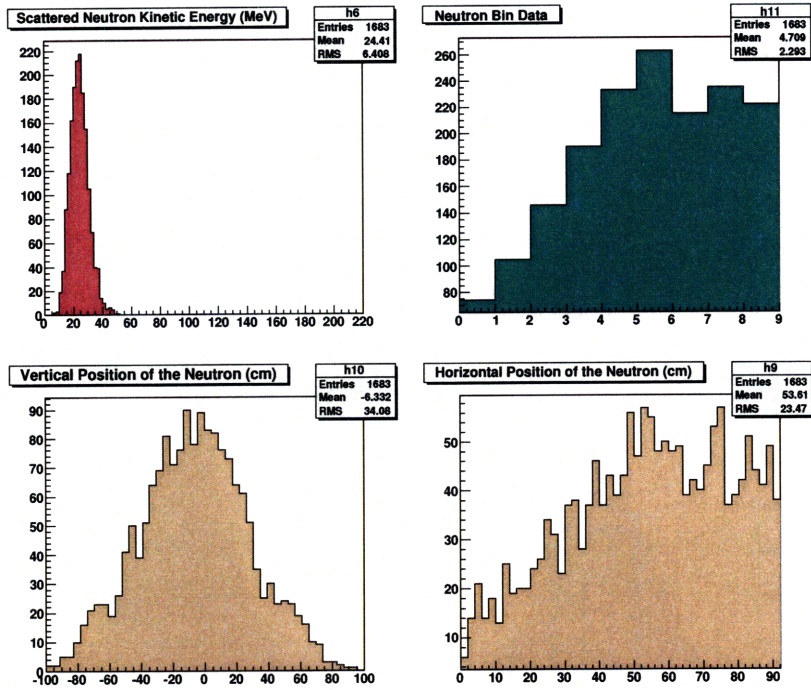


Figure 6-5: Energy, detection location, and bin number of the outgoing neutron in the example simulation.

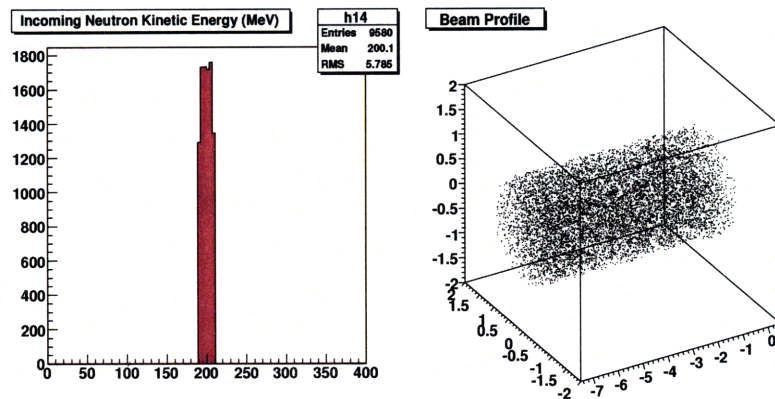


Figure 6-6: The energy of the incoming neutron and the (cylindrical) interaction area in the realistic simulation.

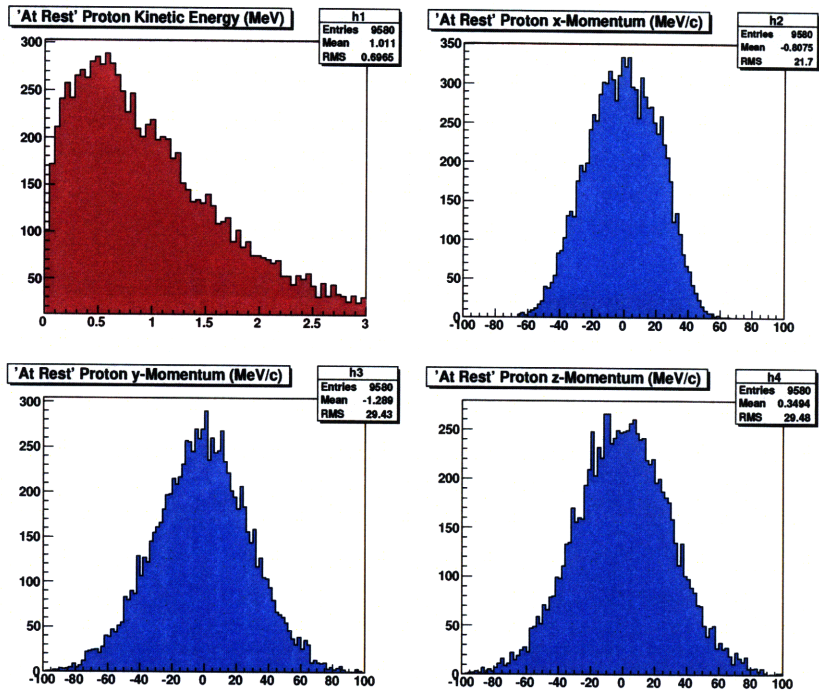


Figure 6-7: Energy and momenta of the “at rest” proton in the realistic simulation.

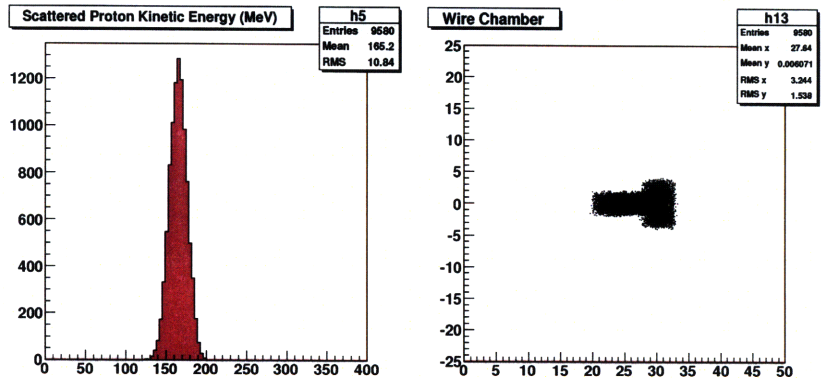


Figure 6-8: Energy and detection location of the ejected proton in the realistic simulation.

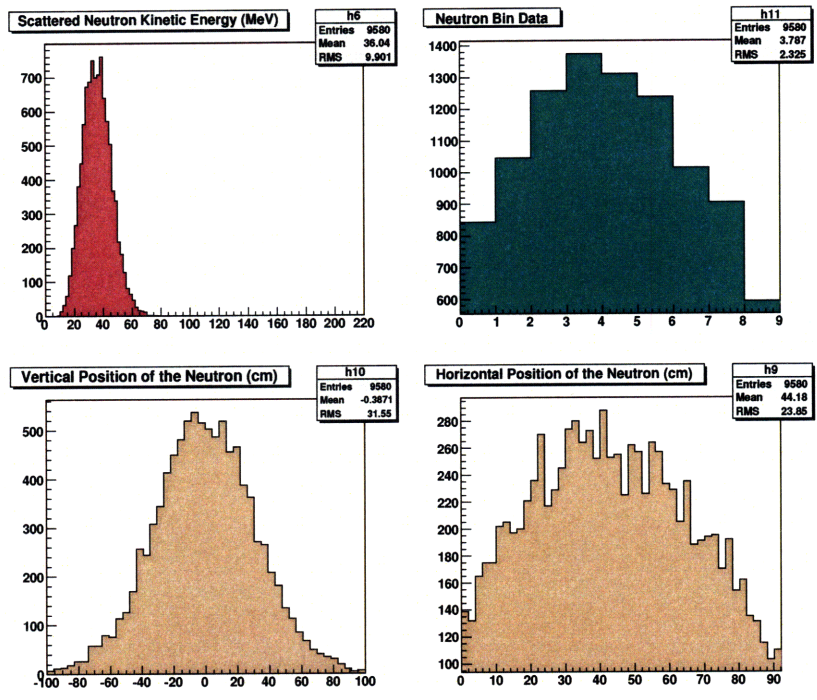


Figure 6-9: Energy, detection location, and bin number of the outgoing neutron in the realistic simulation.

Chapter 7

Results

The goal of this experiment was to measure the energies and scattering angles of the scattered neutron and proton in deuteron breakup. The data will be shown here, both integrated over all incident neutron energies and as a function of incident energy.

The velocity of the incident neutron is determined by the time-of-flight of the neutron to the target plus the TOF of the proton to the dE detector. This approximation is based on the fact that the dE detector is close to the target and at a forward angle, so the proton is carrying most of the incident energy when it strikes the dE detector. The velocity of the scattered proton is given by the difference in TOFs to the dE and P1 detectors. The velocity of the scattered neutron is given by the TOF between the target and the neutron bars. These formulas are shown in Equation 7.1 and the experimental velocity data are shown in Figure 7-1. L_0 , L_{dE} , L_{P1} , and L_a represent the distance from the source to the target and the distances between the target and the dE, P1, and struck (a^{th}) neutron bar, respectively. h is the height on the neutron bar where the event occurred (and 126cm is the height of the beam). TOF_{dE} and TOF_{P1} are the times-of flight between the source and the dE and P1 detectors. TOF_a is the time-of-flight from the source to the a^{th} neutron bar.

$$\begin{aligned}
 v_{in} &= \frac{L_0 + L_{dE}}{TOF_{dE}} \\
 v_p &= \frac{L_{P1} - L_{dE}}{TOF_{P1} - TOF_{dE}} \\
 TOF_n &= TOF_a - L_0/v_{in} \\
 v_n &= \frac{\sqrt{L_a^2 + (h - 126\text{cm})^2}}{TOF_n}
 \end{aligned}
 \tag{7.1}$$

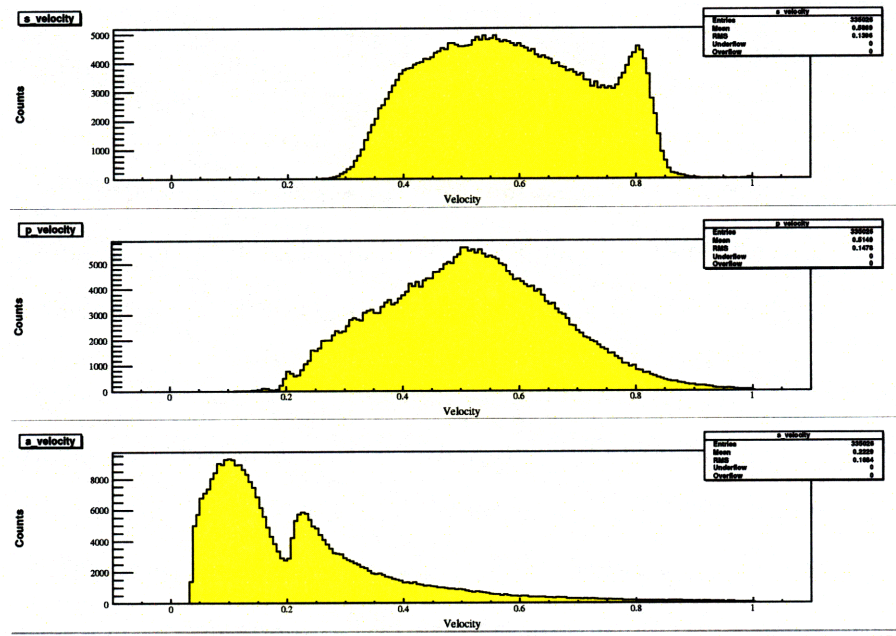


Figure 7-1: The velocities (divided by c) of the incident neutron(top), scattered proton (middle) and scattered neutron (bottom).

The kinetic energies for the three detected particles were calculated using Equation 3.4, and the experimental data are shown in Figure 7-2.

The correlations between scattered proton energy and incident energy, and between scattered neutron energy and incident energy, are plotted in Figures 7-3 and 7-4, respectively.

The neutron scattering angle is determined by the neutron bar that is hit. Thus

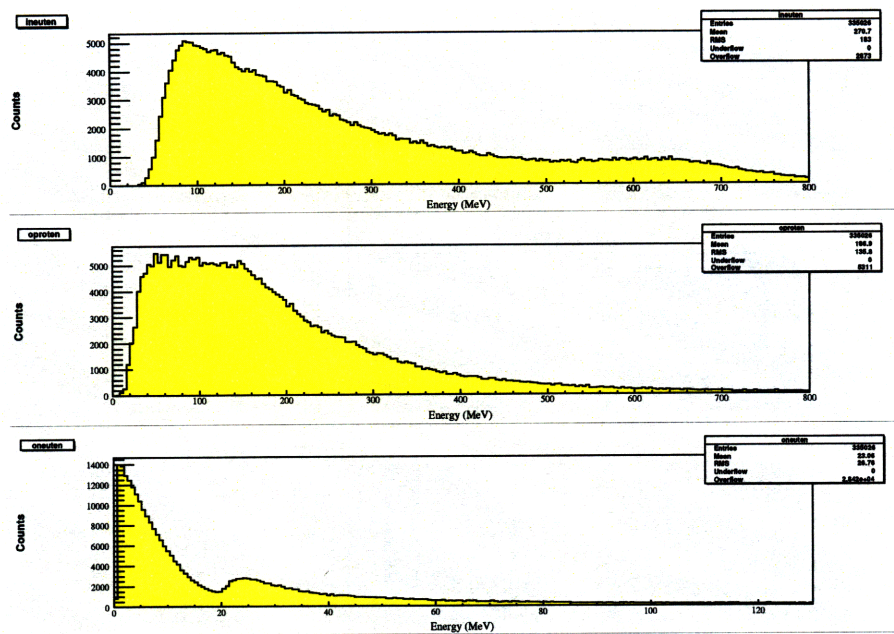


Figure 7-2: The energies of the incident neutron(top), scattered proton (middle) and scattered neutron (bottom).

the distribution of neutron scattering angles is given by a plot of number of events per neutron bar (Figure 7-5).

7.1 $E_{in} = 100MeV$

The data were cut on the range $90MeV < E_{in} < 110MeV$. In this range there were 12542 “good” events. Plots of the resulting energies and velocities and angles, analogous to those above, are Figures 7-6 through 7-8.

The cross section was calculated as described in Chapter 5, and is plotted in Figure 7-9.

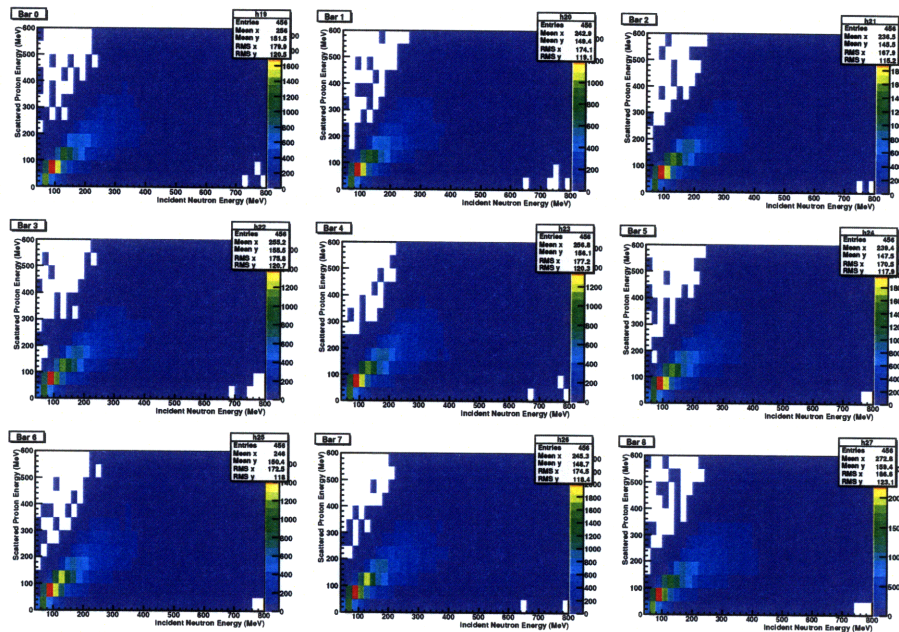


Figure 7-3: The energy of the incident neutron (horizontal axis) plotted against the energy of the scattered proton (vertical axis), for all scattered neutron energies.

7.2 $E_{in} = 200\text{MeV}$

The data were cut on the range $190\text{MeV} < E_{in} < 210\text{MeV}$. In this range there were 5986 “good” events. Plots of the resulting energies and velocities and angles, analogous to those above, are Figures 7-10 through 7-12.

The cross section was calculated as described in Chapter 5, and is plotted in Figure 7-13.

A comparison between the experimental data and the Monte Carlo simulation shows some disturbing discrepancies. The energy spectra observed (Figure 7-11) can be compared with the simulated energies (Figures 6-8 and 6-9), and the neutron bar spectrum from Figure 7-12 can be compared with Figure 6-9. It is troubling that the simulated quasielastic peak in the neutron energy spectrum is between 20 and 60MeV, while the analogous measured peak is between 4 and 12MeV. This may be due to incorrect calibrations; the neutron bar calibrations were particularly subject to error.

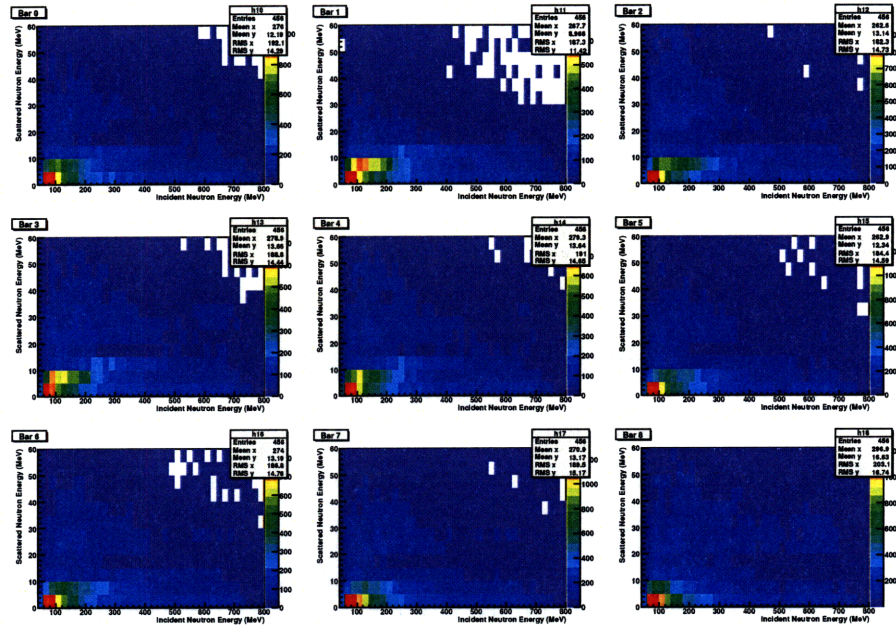


Figure 7-4: The energy of the incident neutron (horizontal axis) plotted against the energy of the scattered neutron (vertical axis), for all scattered proton energies.

When flight times are on the order of nanoseconds, correct energy measurements are extremely sensitive to calibration accuracy. Additionally, the experimental neutron bar spectrum does not show any peak at all. This may be due to additional background events that are not quasielastic scattering, or it may be due to the thresholds on the neutron bar detectors being set at different levels, meaning that the neutron bars did not have the same efficiency.

A similar experiment was carried out in [7], using the reaction $d(p,pn)p$ at 200MeV. In this source, the three-dimensional cross section (with respect to the scattering angles and the energy of the proton) is plotted for many different combinations of angles. The only neutron scattering angle that was comparable between the experiment in [7] and this experiment was for Bar 0, at $\theta_n = 55^\circ$. In [7] there are plots of the cross section at the proton scattering angles $\theta_p = 35^\circ$ and $\theta_p = 45^\circ$ (reproduced in Figures 7-15 and 7-16). The average proton scattering angle in the experiment described here was defined by the acceptance angle of P1, and was around $\theta_p = 25^\circ$. By

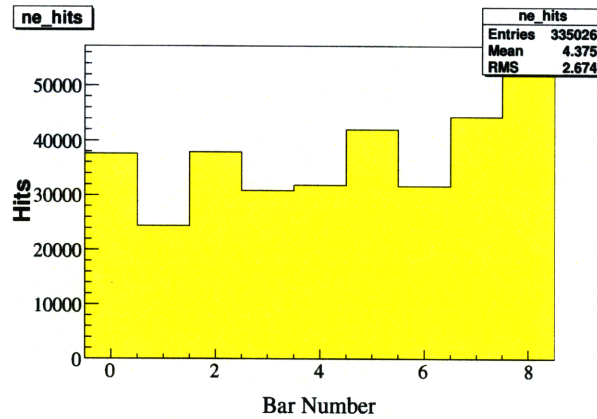


Figure 7-5: The number of events recorded by each neutron bar.

integrating the Bar 0 cross section data from Figure 7-13 over all neutron energies, a comparable plot to those in [7] is obtained (Figure 7-14). The comparison between this experiment and the literature makes sense qualitatively, because the cross section drops off rapidly around $\theta_p = 35^\circ$ (so two orders of magnitude difference between the maximum cross sections at $\theta_p = 35^\circ$ and $\theta_p = 25^\circ$ is not surprising), and it is expected that at small angles the cross section peak should be at a higher energy than at larger angles.

7.3 $E_{in} = 300MeV$

The data were cut on the range $290MeV < E_{in} < 310MeV$. In this range there were 3119 “good” events. Plots of the resulting energies and velocities and angles, analogous to those above, are Figures 7-17 through 7-19.

The cross section was calculated as described in Chapter 5, and is plotted in Figure 7-20.

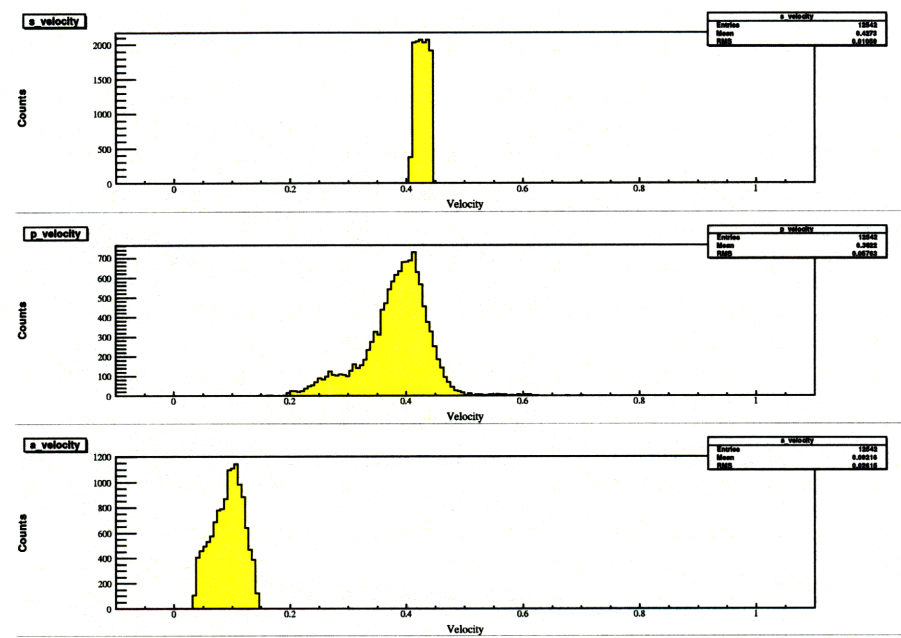


Figure 7-6: The velocities (divided by c) of the incident neutron (top), scattered proton (middle) and scattered neutron (bottom), when the data are cut around 100MeV.

7.4 Error Analysis

As in any experiment, there are a variety of uncertainties in measurements that should be taken into account. Here two such sources of experimental error will be discussed: timing resolution and distance resolution, as they relate to determining the energies of the particles. Other errors include the uncertainty in the solid angle (which is also due to uncertainties in distance resolution), measurements of the detector efficiencies, etc.

The energies of the particles in this experiment were calculated using time-of-flight measurements, from Equation 3.4. The kinetic energy T is a function of the time-of-flight to the detector, and the distance to the detector ($T = f(t, \ell)$). The standard method of propagating error (Equation 7.2), yields the uncertainty in kinetic energy shown in Equation 7.3.

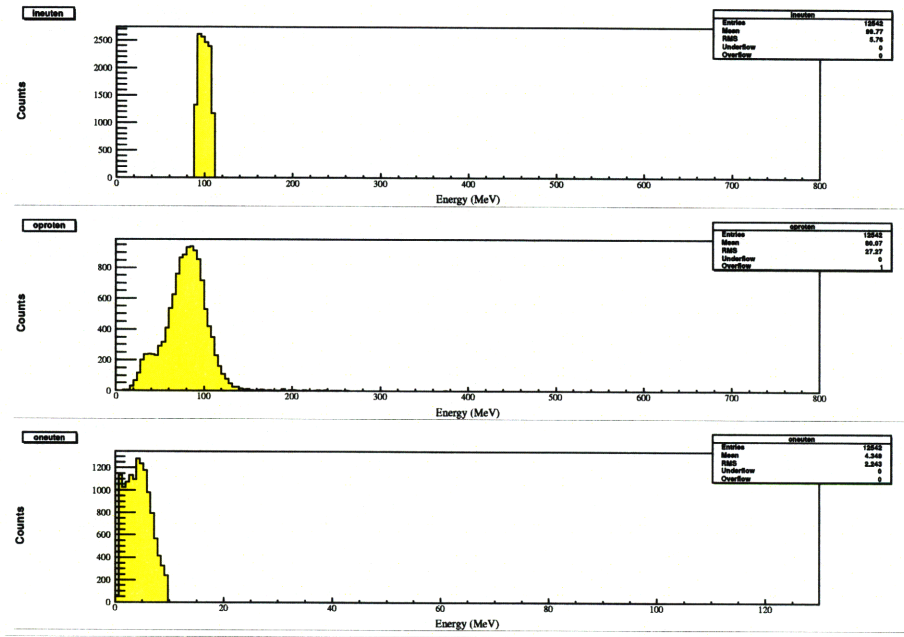


Figure 7-7: The energies of the incident neutron (top), scattered proton (middle) and scattered neutron (bottom), when the data are cut around 100MeV.

$$\sigma_T^2 = \sigma_t^2 \left(\frac{\partial T}{\partial t} \right)^2 + \sigma_\ell^2 \left(\frac{\partial T}{\partial \ell} \right)^2 \quad (7.2)$$

$$\begin{aligned} \sigma_T &= \frac{\ell^2}{t^2 c^2} \frac{m c^2}{(1 - (\ell/t)^2/c^2)} \sqrt{\frac{\sigma_t^2}{t^2} + \frac{\sigma_\ell^2}{\ell^2}} \\ \sigma_T &= \left[\frac{E^3}{(m c^2)^2} - E \right] \sqrt{\frac{\sigma_t^2}{t^2} + \frac{\sigma_\ell^2}{\ell^2}} \\ \sigma_T &= \left[\frac{E^3}{(m c^2)^2} - E \right] \sqrt{\sigma_t^2 \frac{c^2}{d^2} \left[1 - \left(\frac{m c^2}{E} \right)^2 \right] + \frac{\sigma_\ell^2}{\ell^2}} \end{aligned} \quad (7.3)$$

The errors in scattered proton energy, σ_T , as a function of total energy, E , are plotted in Figure 7-21. The distance between the dE and P1 detectors is fixed at $\ell = 146.25\text{cm}$, and the uncertainty in distance is $\sigma_\ell = 0.5\text{cm}$. The timing resolution (σ_t) is about 1ns. As expected, the uncertainty in energy increases dramatically with

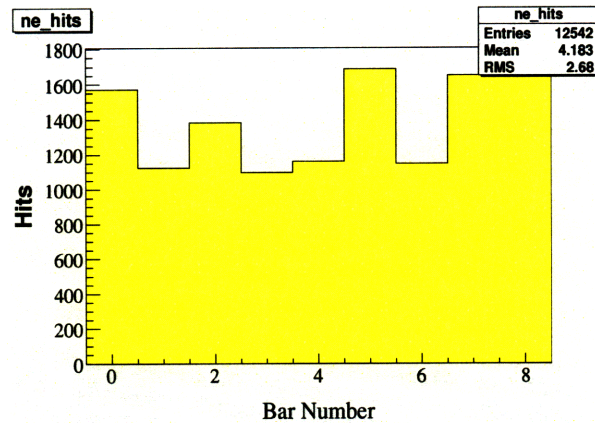


Figure 7-8: The number of events recorded by each neutron bar, when the data are cut around 100MeV.

energy, because higher energies correspond to shorter flight times. The 1ns uncertainty in timing becomes larger compared to the TOF as the TOF shrinks at higher energies. This effect is particularly relevant to measuring the energy of the scattered proton because ℓ and the TOFs are short. This plot indicates two things: First, measuring high scattered proton energies using time-of-flight is entirely unreliable (for example, the error in an 700MeV kinetic energy measurement is 682MeV). Second, the apparent non-conservation of energy from Figure 7-11 (the energy of the scattered proton cannot be 100 MeV higher than the energy of the incident neutron) is consistent with the errors expected at those energies (the error in kinetic energy of a 200MeV scattered proton is 85.6MeV).

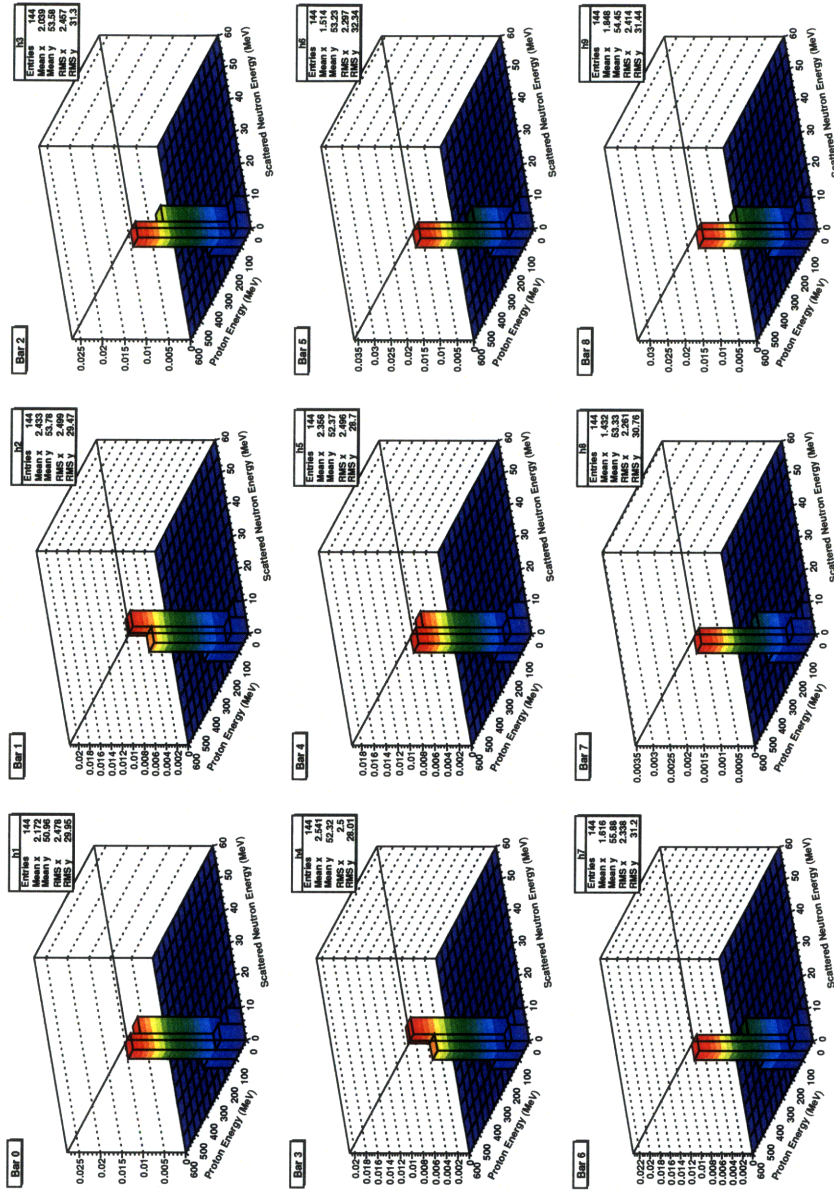


Figure 7-9: The interaction cross section, $\frac{d^4\sigma(E_{in}=100\text{MeV}}{dE_p dE_n d\Omega_p d\Omega_n}$ in $\text{mb/sr}^2/\text{MeV}^2$.

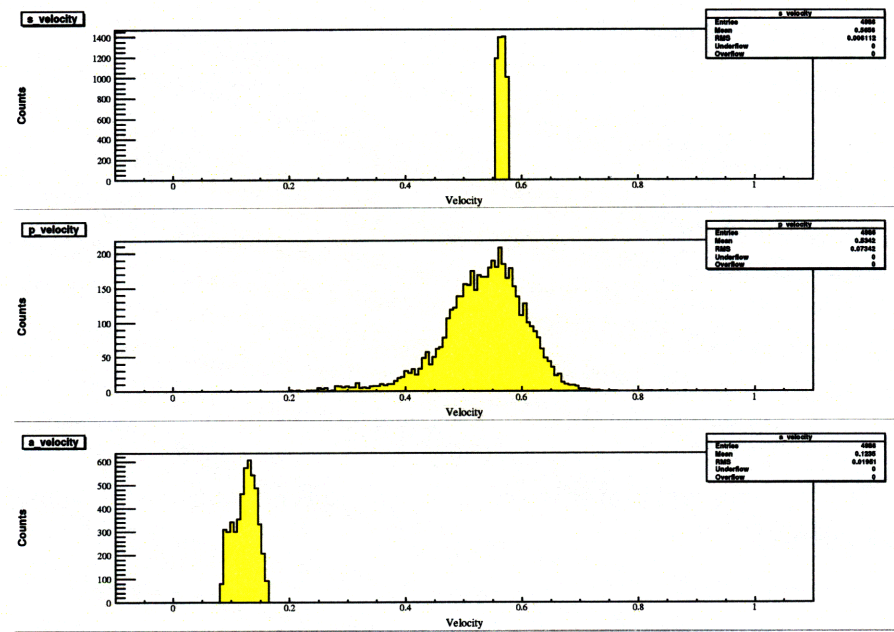


Figure 7-10: The velocities (divided by c) of the incident neutron (top), scattered proton (middle) and scattered neutron (bottom), when the data are cut around 200MeV.

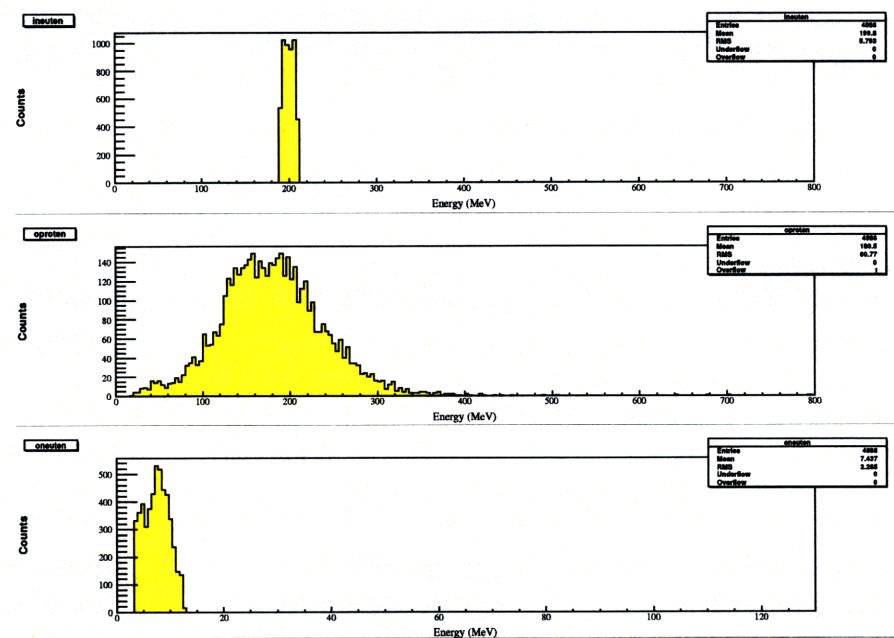


Figure 7-11: The energies of the incident neutron (top), scattered proton (middle) and scattered neutron (bottom), when the data are cut around 200MeV.

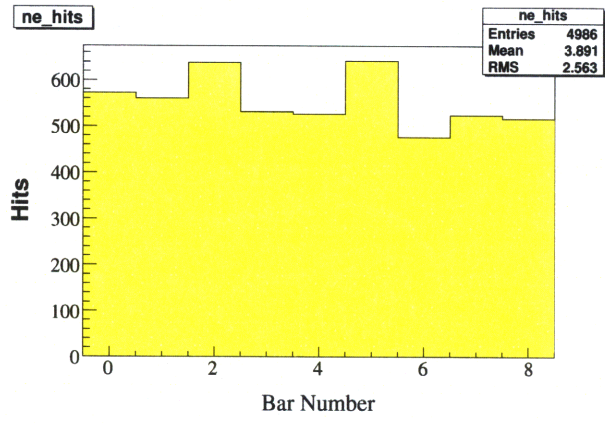


Figure 7-12: The number of events recorded by each neutron bar, when the data are cut around 200MeV.

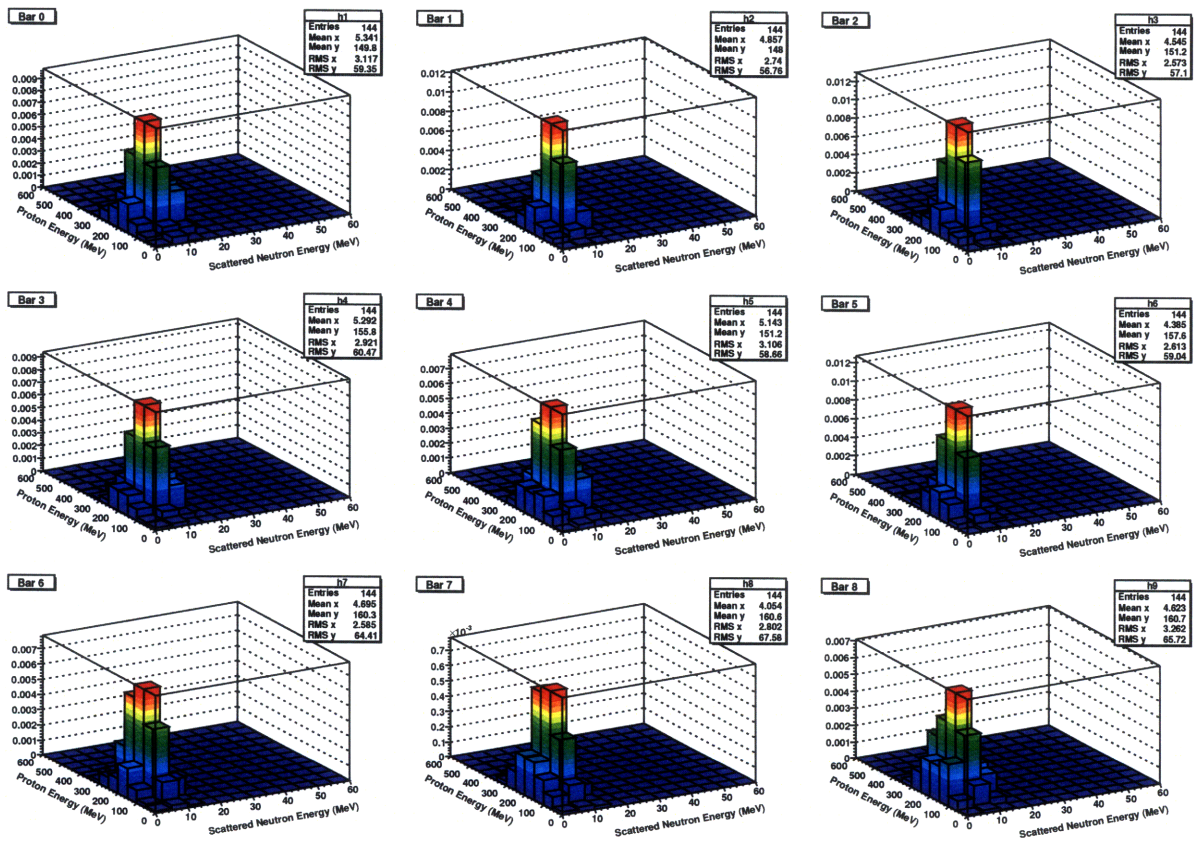


Figure 7-13: The interaction cross section, $\frac{d^4\sigma(E_{in}=200MeV)}{dE_p dE_n d\Omega_p d\Omega_n}$ in $mb/sr^2/MeV^2$.

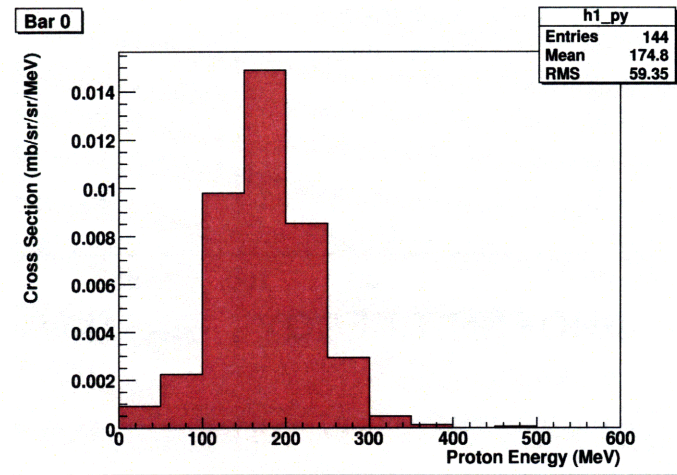


Figure 7-14: The interaction cross section, $\frac{d^3\sigma(E_{in}=200MeV)}{dE_p d\Omega_p d\Omega_n}$ at $\theta_n = 55^\circ$ and $\theta_p = 25^\circ$.

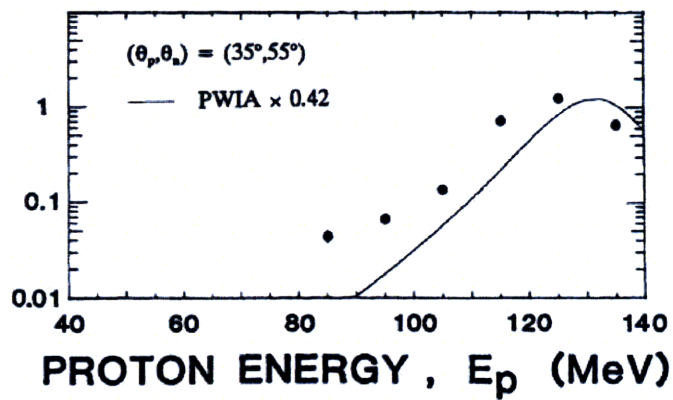


Figure 7-15: The interaction cross section, $\frac{d^3\sigma(E_{in}=200MeV)}{dE_p d\Omega_p d\Omega_n}$ at $\theta_n = 55^\circ$ and $\theta_p = 35^\circ$, in mb/sr²/MeV, from [7].

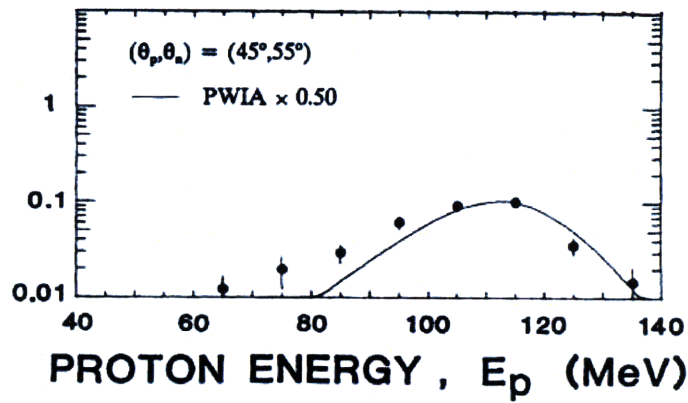


Figure 7-16: The interaction cross section, $\frac{d^3\sigma(E_{in}=200MeV)}{dE_p d\Omega_p d\Omega_n}$ at $\theta_n = 55^\circ$ and $\theta_p = 45^\circ$, in $mb/sr^2/MeV$, from [7].

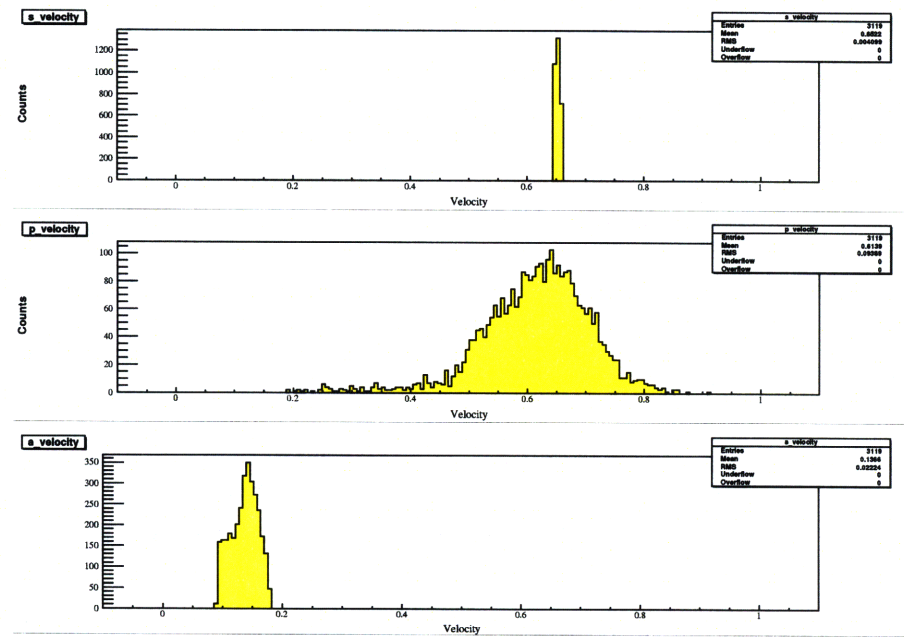


Figure 7-17: The velocities (divided by c) of the incident neutron (top), scattered proton (middle) and scattered neutron (bottom), when the data are cut around 300MeV.

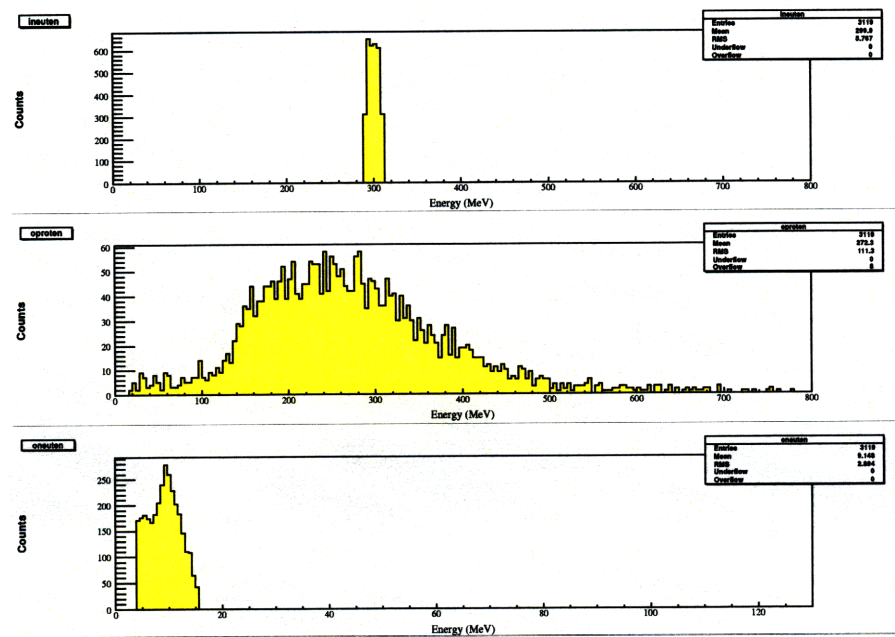


Figure 7-18: The energies of the incident neutron (top), scattered proton (middle) and scattered neutron (bottom), when the data are cut around 300MeV.

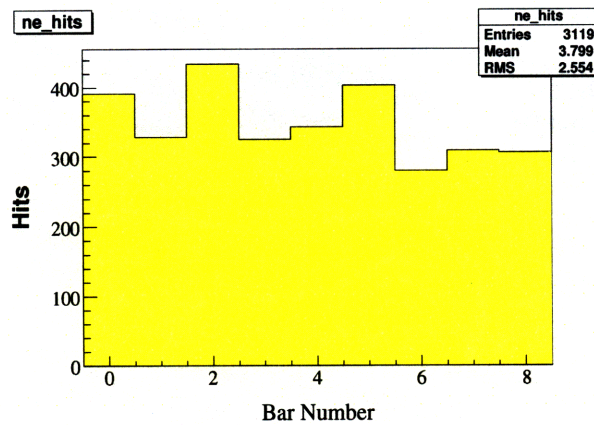


Figure 7-19: The number of events recorded by each neutron bar, when the data are cut around 300MeV.

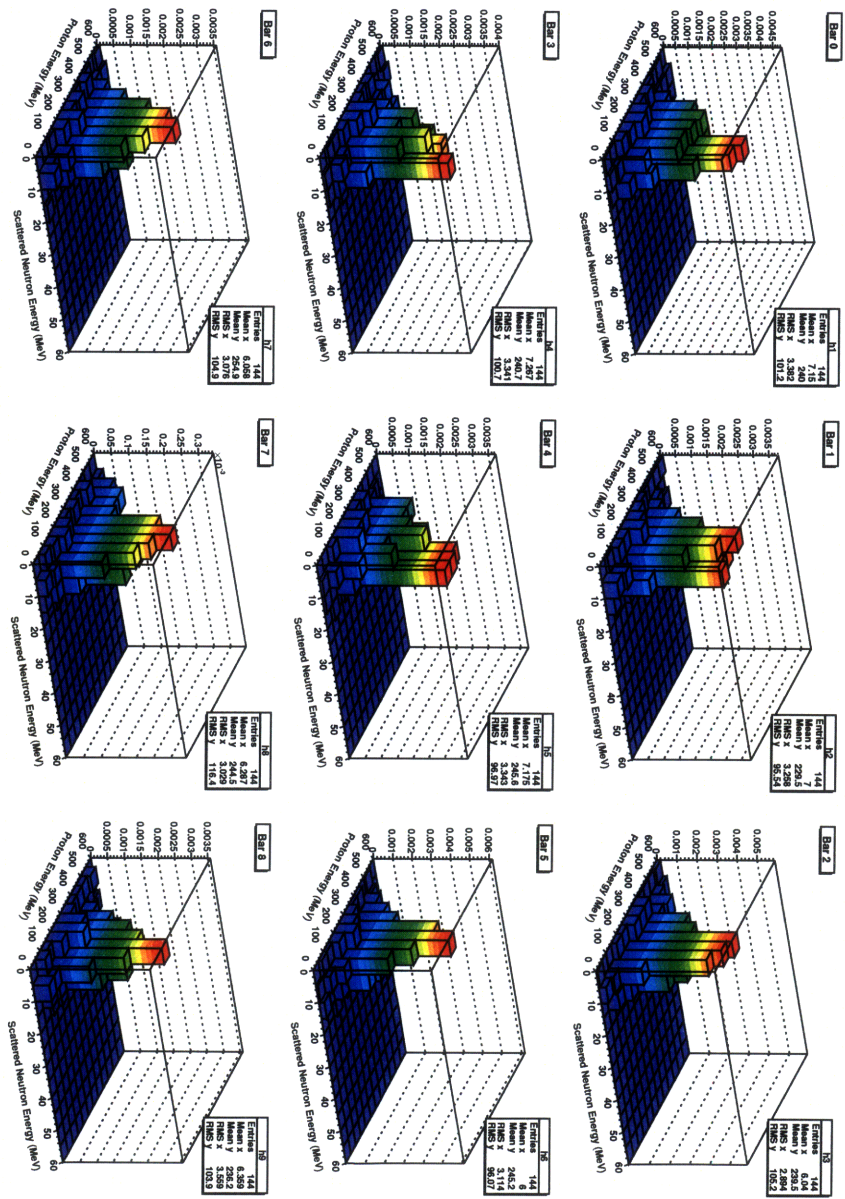


Figure 7-20: The interaction cross section, $\frac{d^4\sigma(E_{in}=300MeV)}{dE_p dE_n d\Omega_p d\Omega_n}$ in $mb/sr^2/MeV^2$.

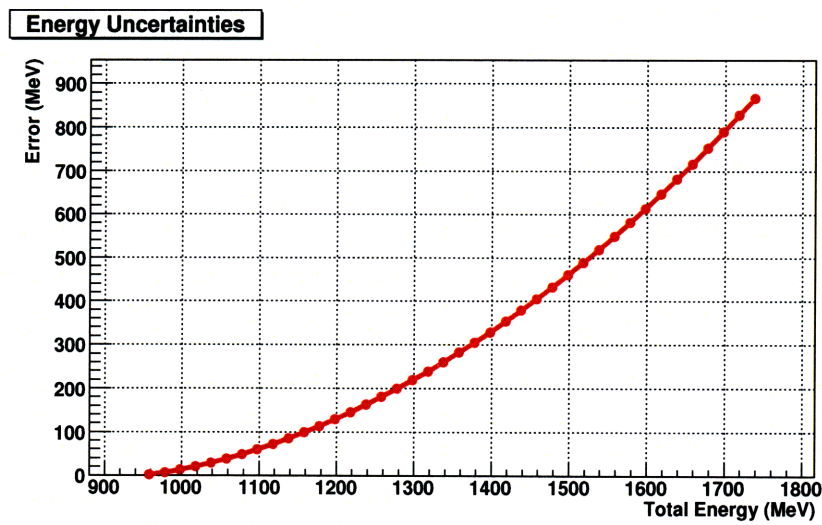


Figure 7-21: The error in energy, σ_T , as a function of total energy, E . Here t is allowed to vary, but ℓ is fixed. (The errors are plotted for kinetic energies between 0 and 800 MeV.)

Chapter 8

Conclusions

In this experiment, neutron-induced deuteron breakup was used to study quasielastic scattering, and perhaps future experiments will use the $d(n,np)n$ reaction to probe the three-nucleon force. Here, the experimental setup consisted of scintillator panels and wire chambers for proton detection and a wall of scintillator bars for neutron detection. A method for calibrating the detectors was described in detail.

There were two main parts of the analysis of this experiment: First, the four-dimensional cross-section was obtained for neutron-deuteron breakup. Second, a Monte Carlo simulation was written to compare quasielastic neutron-proton scattering with quasielastic neutron-deuteron scattering.

Bibliography

- [1] 8.276 class notes, MIT, 18 February 2009.
- [2] Taylan Akdoğan. *Pion Production in the Neutron-Proton Interaction*. PhD dissertation, Massachusetts Institute of Technology, Department of Physics, September 2003.
- [3] M. Bernheim, A. Bussière, J. Mougey, D. Royer, D. Tarnowski, S. Turck-Chieze, S. Frullani, G.P. Capitani, E. de Sanctis, and E. Jans. Momentum distribution of nucleons in the deuteron from the $d(e,e'p)n$ reaction. *Nuclear Physics*, A365:349–370, 1981.
- [4] Kimberly K. Boddy. *Charged-Particle Tracking for Neutron-Deuteron Breakup*. SB thesis, Massachusetts Institute of Technology, Department of Physics, June 2007.
- [5] Maxim B. Chtangeev. *Neutron-Deuteron Elastic Scattering and the Three-Nucleon Force*. MS dissertation, Massachusetts Institute of Technology, Department of Physics, June 2005.
- [6] William R. Leo. *Techniques for Nuclear and Particle Physics Experiments: A How-to Approach*, Section 7.2.3. Springer-Verlag, Berlin, Second Revised edition, 1994.
- [7] W. Pairsuwan, J.W. Watson, M. Ahmad, N.S. Chant, B.S. Flanders, R. Madey, P.J. Pella, and P.G. Roos. Analyzing powers for the ${}^2\text{H}(p,pn){}^1\text{H}$ reaction at 200 MeV. *Physical Review C*, 52(5):2552–2558, November 1995.
- [8] William H. Press, Saul A. Teukolsky, William T. Vetterling, and Brian P. Flannery. *Numerical Recipes in C: The Art of Scientific Computing*, Section 7.2. Cambridge University Press, Cambridge, Second edition, 1992.